Department of Physics and Astronomy

University of Heidelberg

Master thesis

in Physics

submitted by

Daniel Linnemann

born in Hamm

2013

Realization of an SU(1,1) Interferometer with Spinor Bose-Einstein Condensates

This master thesis has been carried out by Daniel Linnemann

at the

Kirchhoff-Institute for Physics

under the supervision of

Prof. Dr. Markus K. Oberthaler

Realization of an SU(1,1) Interferometer with Spinor Bose-Einstein Condensates

An SU(1,1) interferometer is obtained from a Mach-Zehnder interferometer by replacing both its beam splitters with parametric amplifiers. These new beam splitters are characterized by a non-linear response to a strong coherent pump beam and produce entangled photon pairs in its side, viz signal and idler, modes.

In quantum atom optics, a parametric amplifier can be realized by means of spin-changing collisions. During these collisions atoms from a single spin component are pairwise scattered into side modes. As a coherent process these collisions are reversible and are utilized in the SU(1,1) interferometer as both a beam splitter as well as a beam combiner. Highest phase sensitivity of such an interferometer is achieved when the second period of spin-changing collisions completely reverses the effect of the first. At this point the initial vacuum mode is recovered at the output and Heisenberg limited phase estimation can be obtained.

We report on the experimental implementation of an SU(1,1) interferometer using Rb-87 atoms in the $F = 1$ ground state. We observe the phase-dependent output signal for small average atom numbers inside the interferometer and characterize its phase sensitivity.

Realisierung eines SU(1,1) Interferometers mit Spinor Bose-Einstein Kondensaten

Ein SU(1,1) Interferometer erhält man durch den Austausch beider Strahlteiler eines Mach-Zehnder Interferometers mit parametrischen Verstärkern. Diese neuen Strahlteiler zeichnen sich durch eine nichtlineare Antwort auf einen starken, kohärenten Pumpstrahl aus und produzieren verschränkte Photonenpaare in ihren Seiten-, also „Signal“- und „Idler“-, Moden.

In der Quantenatomoptik kann ein parametrischer Verstärker durch spinaustauschende Stöße realisiert werden. Im Verlauf dieser Stöße werden Atome aus einer einzelnen Spinkomponente paarweise in Seitenmoden gestreut. Als kohärenter Prozess sind diese Kollisionen reversible und in einem SU(1,1) Interferometer werden sie sowohl als Strahlteiler als auch als Strahlkombinierer genutzt. Höchste Phasensensitivität eines solchen Interferometers wird erreicht, wenn die zweiten spinaustauschenden Kollisionen den Effekt der ersten rückgängig machen. Unter diesen Umständen erhält man das anfängliche Vakuum am Eingang auch am Ausgang und Phasensensitivität am Heisenberg-Limit ist möglich.

Wir berichten über die experimentelle Implementierung eines SU(1,1) Interferometers mit Rb-87 Atomen, die in ihrem $F = 1$ Grundzustand sind. Wir beobachten das phasenabhängige Ausgangssignal für kleine mittlere Atomzahlen im Interferometer und bestimmen die Phasensensitivität.

Contents

Introduction

Interferometry and the Heisenberg sensitivity limit

Interferometry is concerned with estimating the differential phase accumulated between (usually) two states. Its ubiquitous use in science and technology is the consequence of at least three characteristics: the plethora of physical processes expressing themselves in phase differences; the exceptional high precision obtainable in determining these phases; and its conceptually very simple working principle: When a known quantum state is fed into the interferometer, a differential phase shift φ can be estimated by comparing the output signal to the known input. Quite intuitively the phase change can be determined the better, the greater the difference between input and output is. We can quantify this by introducing the infinitesimal distance d_H of two quantum states [1]: $d_H^2 = \arccos^2 \mathcal{F} = 1 - \mathcal{F}^2$ [2]. Here $\mathcal{F}$ denotes the fidelity of the two states $|\Psi_{\text{in}}\rangle$ and $|\Psi_{\text{out}}\rangle$ which shall be distinguished, $\mathcal{F} = |\langle\Psi_{\text{in}}|\Psi_{\text{out}}\rangle|$. $\mathcal{F}^2$ is the probability of mistaking the state $|\Psi_{\text{in}}\rangle$ for state $|\Psi_{\text{out}}\rangle$in a single measurement. In the case of coherent states d_H corresponds to the angle between both states in a Bloch sphere picture [3].

As a prototypical example we might consider the Mach-Zehnder interferometer, as shown in Figure 1. Starting from the probe state $|\Psi_{\text{in}}\rangle$, a phase difference φ between both arms is accrued, thereby rotating the input state by an angle φ on the Bloch sphere. The connection between interferometric sensitivity and change of distance is made by means of the Cramer-Rao bound. This relation states that the minimal achievable phase uncertainty $\langle(\Delta\varphi)^2\rangle$ is bounded by the inverse Fisher information F, given in turn by the change of distance with the parameter [4]:

$$\langle(\Delta\varphi)^2\rangle \geq 1/F \ , \quad \text{with} \quad F = \frac{\mathrm{d}d_H^2}{\mathrm{d}\varphi^2}$$

If the interferometer is fed with N identical and non-entangled particles, $\mathcal{F}^2 = \left|\langle\Psi_{\text{in}}|^{\otimes N} |\Psi_{\text{out}}\rangle^{\otimes N}\right|^2 = \cos^{2N}\varphi$. For small angles, we have $\cos^{2N}\varphi = 1 - N\varphi^2 + \mathcal{O}(\varphi^4)$ and thus $F \leq N$. This basically reformulates the square-root-law, $\langle\Delta\varphi\rangle = 1/\sqrt{N}$, known from statistics for independent observations. Since the input state is separable, we can also interpret a single measurement with N particles as N single measurements. By introducing correlations between particles, this limit, also known as the standard quantum limit, can be surpassed, thereby allowing for more efficient phase estimations. For linear interferometers the fundamental limit is set by $\langle(\Delta\varphi)^2\rangle = 1/N^2$ [5] known as the Heisenberg-limit. To attain this limit one requires maximally entangled states [6] which are very fragile. Non-linear interferometers relax the requirements on the level of entanglement [7] and are thus a promising candidate to demonstrate sensitivity at the Heisenberg limit in experiments with ultracold gases.

In this work we will describe the realization of such a non-linear interferometer. It has already been proposed and studied theoretically in the realm of optics in the 1980s to harness the at the time new non-linear media by [8], who called it an SU(1,1) Mach-Zehnder interferometer. The key idea is to exchange the beam splitters of a Mach-Zehnder by non-linear crystals. The response of these crystals to a strong pump beam is characterized by harmonics different to the fundamental (pump) frequency. In particular they allow parametric down-conversion, whereby a photon of the pump beam is converted into a pair of (lower energetic) photons as long as energy and momentum are both conserved. Quantum mechanically one might also interpret the process as an amplifier, which intensifies the

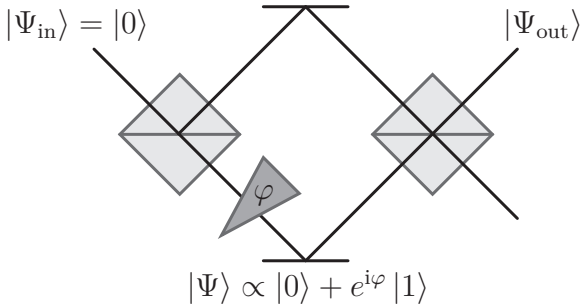

Figure 1: Mach-Zehnder interferometer. The input state $|\Psi_{\text{in}}\rangle$ is divided into two paths by a beam splitter. A phase-shifting element affects both paths differently, before they are reunited by a second beam-splitter. The entire interferometer constitutes a rotation of $|\Psi_{\text{in}}\rangle$ by an angle φ on the Bloch-Sphere.

ever-present vacuum fluctuations such that a pair of real photons is created. In this sense the non-linear medium becomes an active one. Due to their joint creation these photons are highly correlated with each other, albeit each might travel in different direction. [8] showed that these entangled photon pairs can be used to achieve phase estimation at the Heisenberg-limit.

The Mach-Zehnder interferometer uses passive beam splitters and is thus described by the rotational group SU(2), encoding the conservation of energy. It is this conservation of energy which constrains its effect to rotations on a fixed-radius Bloch sphere, as stated above. In contrast the non-linear interferometer uses active media, thereby violating energy conservation and unitary evolution. This interferometer is described by the symmetry group SU(1,1) and is therefore called an SU(1,1) interferometer [8]. Spinor Bose-Einstein condensates provide a very similar mechanism to parametric down-conversion [9, 10]. This mechanism has already been used to create entangled states of massive particles, which when fed into the atomic counterpart [11, 12] of a conventional optical Mach-Zehnder interferometer outperform classical states [13].

General idea of an implementation in ultracold gases

In a homogenous magnetic field, the magnetic quantum number m is a strictly conserved quantity. In collisions between atoms, however, each individual atom may be scattered into states with different magnetic moment – as long as their combined magnetic moment remains unaltered. We use this very fact to produce entangled pairs of massive atoms, which when used in an interferometer surpass the classical sensitivity limit. ^{87}Rb atoms in their ground state manifold have spin $F = 1$ and thus only three possible orientations of spin. We prepare hundreds of atoms in a pure $|0\rangle \equiv |F = 1, m_F = 0\rangle$ Bose-Einstein condensate. Atom pairs are subsequently produced by sustained scattering of two $|0\rangle$ atoms into states $|1\rangle \equiv |1, 1\rangle$ and $|-1\rangle \equiv |1, -1\rangle$, respectively: $|0\rangle + |0\rangle \rightarrow |+1\rangle + |-1\rangle$. At these ultracold temperatures individual collisions become collective and coherent due to the very limited phase space attainable. With initially empty modes $|\pm 1\rangle = |\text{vac}\rangle$ this process acts as an non-linear amplifier [14, 15], which will provide the foundation for an active SU(1,1) interferometer.

Outline of this thesis

In the first section we will detail the experimental system and introduce the theoretical description of spinor Bose-Einstein condensates. The Hamiltonian of spin-changing collisions will be discussed especially from the perspective of how to experimentally gain control over these collisions. Having discussed the experimental techniques to use spin-exchange as a well-isolated beam splitter we will study its quantum effect in the second section.

The third section is finally devoted to the SU(1,1) interferometer. Its appearance resembles the Mach-Zehnder interferometer but uses spin-exchange as beam splitters. In this section, the previous discussion of spin-exchange will be put into context and we will discuss the constituents of the SU(1,1) interferometer in detail. Special attention will be paid to phase shifting elements and the interferometer's performance on measuring these phases. We will study the phase sensitivity both, theoretically as well as experimentally and give an account of technical limitations.

Most importantly, as this is very much work in progress only started two months ago, we will conclude with an agenda of how to pursue further. The work which has been done in the remainder of the year is not part of this thesis and will be published elsewhere [16].

1 Experimental techniques and Hamiltonian

1.1 Studying spinor dynamics in an optical lattice

We consider ^{87}Rb atoms in their ground state manifold, $F = 1$, confined in a tight optical trap [18]. This trap is composed of an optical dipole trap beam with superimposed lattice beams, as shown in Figure 2. The dipole trap beam captures the atoms along its axis but only provides very shallow confinement on-axis, since the aspect ratio of on-axis to radial trap frequency is about 50. Additionally, two lattice beams are crossed under an angle of $9\,^\circ$ and interfere to yield a one-dimensional lattice with lattice spacing of $\lambda_l = 5.5\,\mu\text{m}$. The trap frequency sets the highest energy scale and the spin-healing length is larger than the extent of the wave function at each lattice site. Then the external motion is frozen and all dynamics happen exclusively in the internal degrees of freedom. This situation is known as the single (spatial)-mode approximation [19, 20]. On the timescale of our experiments no tunnelling takes place between adjacent lattice sites for the reason of both high inter-well potential and large lattice spacing. The trapping potential is in good approximation independent of the internal degrees of freedom, thus allowing to study spinor dynamics.

1.2 Hamiltonian of $F = 1$ spinor Bose-Einstein condensates

In dilute ultracold gases, we only have to consider binary collisions between particles. The scattering potential is then solely described by the s-wave scattering length c_{F_c}, which depends on the total angular momentum F_c the two individual $F = 1$ atoms couple to [19–22]. This is either $F_c = 2$ or $F_c = 0$ due to bosonic symmetry requirements. Noting that the operator $\boldsymbol{F}_1 \cdot \boldsymbol{F}_2$ has eigenvalue 1 for $F_c = 2$ and eigenvalue -2 for $F_c = 0$, we can write the interaction term as

$$V \propto (2c_2 + c_0) + (c_2 - c_0)\boldsymbol{F}_1 \cdot \boldsymbol{F}_2$$

For ^{87}Rb the scattering length $c_0(c_2)$ is about 102(100) Bohr radii, such that $(c_2 - c_0) < 0$. For angular momentum operators

$$\boldsymbol{F}_1 \cdot \boldsymbol{F}_2 = F_{1,z}F_{2,z} + \frac{1}{2}(F_{1,+}F_{2,-} + F_{1,-}F_{2,+}) \tag{1}$$

holds where $F_{i,\pm}$ denote the ladder operators for the i-th angular momentum. The second term in this decomposition really spells out the production of correlated pairs whereby, starting from atoms in state $|0\rangle$ a pair atom state is produced with exactly one atom in the $|1\rangle$ and the other in the $|-1\rangle$ state. Similar to the Schwinger representation for two modes we can construct angular momentum operators for the three levels of $F = 1$ which will become useful later on:

$$\begin{aligned} F_- &= a_\uparrow^\dagger a_0 + a_0^\dagger a_\downarrow & F_x &= \frac{1}{2}(F_+ + F_-) \\ F_+ &= a_0^\dagger a_\uparrow + a_\downarrow^\dagger a_0 & F_y &= \frac{1}{2\mathrm{i}}(F_+ - F_-) \\ & & F_z &= a_\downarrow^\dagger a_\downarrow - a_\uparrow^\dagger a_\uparrow \end{aligned} \tag{2}$$

Here $a_{\uparrow(\downarrow)}$ denotes the annihilation operator for the mode $|+1\rangle$ ($|-1\rangle$) (from now on called side modes) and a_0 is the corresponding operator for the pump mode $|0\rangle$. Due to symmetry

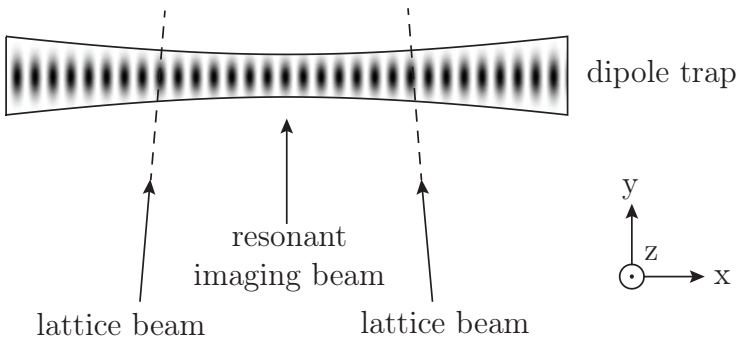

Figure 2: Setup of the optical lattice in which all experiments are performed. A strong dipole trap laser at $\lambda = 1030\,\mathrm{nm}$ captures the atoms along the x-direction, while providing only very weak confinement on its axis. The ratio of transverse to longitudinal trap frequencies is about 50. Two lattice beams at $\lambda = 820\,\mathrm{nm}$ cross under an angle of $9\,^\circ$ yielding a standing wave potential with $\lambda_l = 5.5\,\mu\mathrm{m}$. The atoms are trapped in the anti-nodes of the intensity pattern. Resonant light is used for lattice site resolved absorption imaging [17]. This imaging is irrespective of the internal state. To account for the internal state a magnetic field gradient in z-direction serves as a Stern-Gerlach pulse to spatially separate the three magnetic sublevels of the ^{87}Rb atoms in their ground state manifold $F = 1$.

arguments the Hamiltonian can be cast into a form which shows the collective behaviour arising from these individual collisions [23].

$$\mathcal{H} = \frac{(c_2 - c_0)}{2} L^2$$

Here L is a spin of size N composed of the N individual spin-1 particles and all constant terms ($\propto N = N_0 + N_\uparrow + N_\downarrow$ and N^2) have been dropped. Of course, L^2 can also be represented in terms of ladder-operators and equation (1) holds as well. The much larger combined spin now allows for the production of many atom pairs. In our case of an initially pure $m_F = 0$ condensate, we have $L_z = 0$ for all times, since L_z is an conserved quantity of the ladder operators. Together with equation (2) we can then reformulate the Hamiltonian as [24]

$$\mathcal{H} = \mathcal{H}_{\mathrm{inel}} + \mathcal{H}_{\mathrm{el}} \qquad \text{with} \qquad \begin{aligned} \mathcal{H}_{\mathrm{inel}} &\propto (c_2 - c_0)\left(a_0 a_0 a_\uparrow^\dagger a_\downarrow^\dagger + a_0^\dagger a_0^\dagger a_\uparrow a_\downarrow\right) \\ \mathcal{H}_{\mathrm{el}} &\propto (c_2 - c_0)(2N_0 - 1)(N_\uparrow + N_\downarrow) \end{aligned} \tag{3}$$

For very short times, we can assume the pump mode to be undepleted and perform a Bogoliubov approximation: $a_0 |N_0\rangle = a_0^\dagger |N_0\rangle = \sqrt{N_0}\,|N_0\rangle$, $N_0 \gg 1$ [25]. Then

$$\mathcal{H}_{\mathrm{inel}} = (c_2 - c_0) N_0 (a_\uparrow^\dagger a_\downarrow^\dagger + \mathrm{h.c.}) \tag{4}$$

While H_{inel} produces the desired pairs the term $\mathcal{H}_{\mathrm{el}}$ leads in principle to a phase mismatch between the pump and side modes: Whereas the phase evolution of a_0 due to H_{el} is given by $\exp(N_\uparrow + N_\downarrow)$ with $N_\uparrow + N_\downarrow \approx 0$, both, $a_\downarrow$ and $a_\uparrow$ evolve with $\exp N_0$ [26]. As it turns out the mean-field shift responsible for $\mathcal{H}_{\mathrm{el}}$ is very small, but terms of the same form will become important later on.

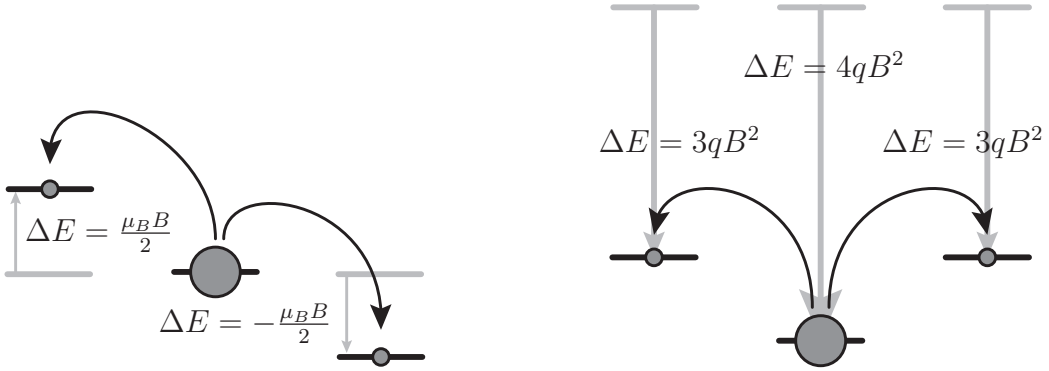

(a) Linear Zeeman effect **(b)** Quadratic Zeeman effect

Figure 3: Energy levels of the ground state manifold of ^{87}Rb in a magnetic field. The linear Zeeman effect as depicted in **a)** does not affect the spin-changing collisions, since the energy gained by one particle has to be spent by the other, $\mu_B = 2 \cdot 700\,\frac{\mathrm{kHz}}{\mathrm{G}}$. The quadratic Zeeman effect shifts the levels of $F = 1$ energetically down. However, the pump mode is shifted further than the side modes by $q = 72\frac{\mathrm{Hz}}{G^2}$. This can be used to control the spin-exchange.

1.3 Experimental control

The Hamiltonian supports the production of perfectly correlated atom pairs by means of the term $\mathcal{H}_{\mathrm{inel}} = a_0 a_0 a_\uparrow^\dagger a_\downarrow^\dagger + \mathrm{h.c.}$ which we would like to harness. We thus need to find ways to experimentally control the process. In particular we need to be able to turn it on and off at will to realize a well isolated non-linear beam splitter.

1.3.1 Magnetic fields

The Zeeman effect adds a term $\mathcal{H}_\mathcal{B} \propto BL_z$ to the Hamiltonian. As we have already seen above, all terms proportional to L_z do not influence the spin-changing collisions. Besides the linear shift in a magnetic field there are, however, also higher order terms. These come about due to the mixing of states in the upper $F = 2$ and lower $F = 1$ manifold, since F is only an approximate quantum number in a small magnetic field. The Breit-Rabi formula considers these effects and yields the so-called quadratic Zeeman effect: It shifts the levels of the $F = 1$ manifold of ^{87}Rb energetically down, see Figure 3 b). The differential energy shift between $|1, 0\rangle$ and $|1, \pm 1\rangle$ is $q = 72\mathrm{Hz}/G^2$. The Hamiltonian can thus be supplemented with $\mathcal{H}_{B^2} = qB^2(N_\uparrow + N_\downarrow)$, which is of the same form as $\mathcal{H}_{\mathrm{el}}$ and can be used to stop the effect of $\mathcal{H}_{\mathrm{inel}}$ by introducing a phase mismatch as discussed above.

This situation is different to the $F = 2$ manifold of ^{87}Rb . For the upper manifold the mean-field shift is larger and $\mathcal{H}_{\mathrm{el}}$ needs to be compensated in order to start spin-changing collisions [27]. This can be done for instance by a magnetic field [28], since the mean-field shift
well characterized state where all atoms are in $|0\rangle$ at high field, spin-exchange might be initiated by quenching the magnetic field down to almost zero [29]. However, to realize two well isolated beam splitters, ramping up and down magnetic fields lacks the necessary control and speed. Instead we use microwave dressing.

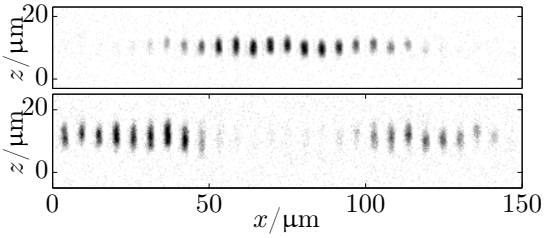

Figure 4: Typical experimental picture illustrating the magnetic field gradient over the extent of the optical lattice. Shown is the outcome of a Ramsey sequence [12] with 30 ms evolution time between states $|2,-2\rangle$ (upper panel) and $|1,-1\rangle$. This transition is three times linearly Zeeman sensitive, $\Delta E = 3 \cdot \frac{\mu_B}{2} B$. The magnetic field gradient amounts to about 100 μG over the entire lattice at a magnetic field of $B = 1.56$ G. Absorption imaging of the $F = 2$ and $F = 1$ manifold are done in sequence which is why for the $F = 1$ image the clouds are more dilute due to the longer time of flight.

1.3.2 Microwave dressing

By state selective microwave dressing, we can initiate and maintain the spin-changing collisions both very quickly and in a controlled manner [30]. Coupling two states by coherent microwave radiation with the resonant Rabi frequency Ω and the detuning Δ to the atomic resonance is described by the Hamiltonian [31]

$$\mathcal{H} = \frac{1}{2}(\Omega\sigma_x - \Delta\sigma_z) \approx \frac{1}{2}\left(\sqrt{\Omega^2 + \Delta^2} - \Delta\right)\sigma_z$$

with the Pauli-matrices σ_i. The approximation is valid for far-off resonant driving, $\Delta \gg \Omega$ and we have $\mathcal{H} \approx \frac{\Omega^2}{4\Delta}\sigma_z$, which means that the levels are shifted in energy by

$$\Delta E = \pm\frac{\Omega^2}{4\Delta} \tag{5}$$

respectively. We employ microwave dressing of the $|1,0\rangle$ state by coupling it off-resonantly to the $|2,0\rangle$ state. The resonance frequency of this π transition occurs only once in the entire level scheme which minimizes the effect of other perturbing level couplings, see Figure 5. Both $m = 0$ states do not shift linearly in a magnetic field and are only affected via the second order Zeeman effect. The microwave dressing is thus mostly immune to magnetic field noise. Microwave dressing supplements the Hamiltonian with $\mathcal{H}_\Omega = -\frac{\Omega^2}{4\Delta}N_0$. Dropping constant terms, this can also be written as $\mathcal{H}_\Omega = \frac{\Omega^2}{4\Delta}(N_\uparrow + N_\downarrow)$ which can be used to compensate for terms due to the quadratic Zeeman effect (and $\mathcal{H}_{\mathrm{el}}$). Additionally, by either red or blue detuning the microwave to atomic resonance the energy level can be shifted up and down.

1.4 Experimental sequence

We magnetically trap [32] ^{87}Rb atoms in the $|1,-1\rangle$ state before transferring them into a crossed dipole trap. The light intensity is subsequently reduced to evaporatively cool the atoms to a temperature of a few 10 nK, well below the transition temperature to a Bose-Einstein condensate [33]. Adiabatically ramping down one of the crossed dipole laser beams lets the condensate spread along the axis of the remaining dipole trap beam. This

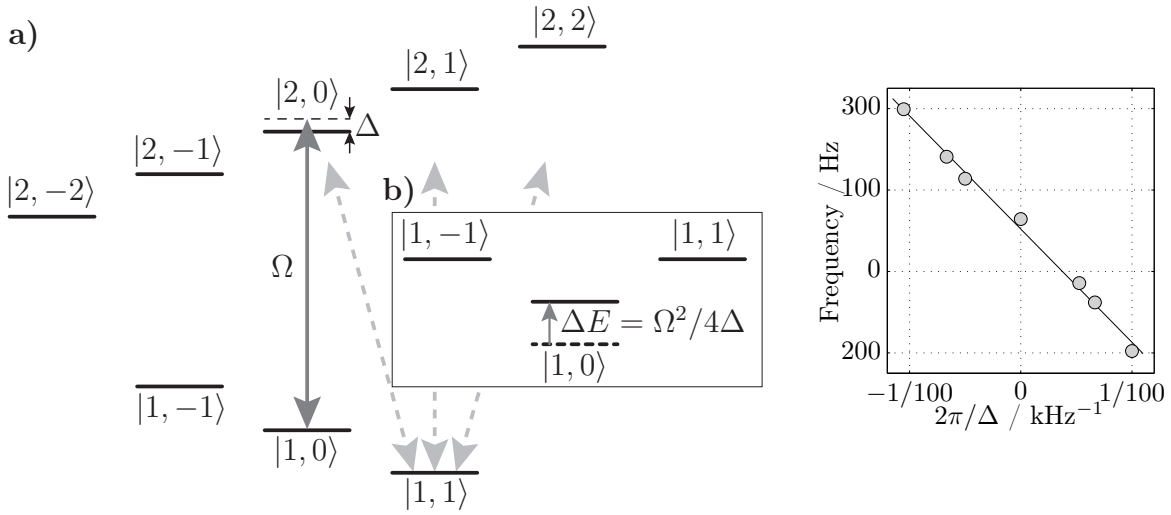

Figure 5: Microwave dressing of the $|1,0\rangle$ state. **Left)** a) The energy shift due to the linear Zeeman effect is 700 $\frac{\text{kHz}}{\text{G}}$ and is much larger than the detuning Δ used for microwave dressing, such that the coupling of other states is negligible. The inset b) shows the effect of the microwave dressing when only the second order Zeeman effect is considered. **Right)** Observed level shifts in a Ramsey sequence between $|1,0\rangle$ and $|2,0\rangle$. The fit of the form $\Delta E/2 = \frac{\Omega^2}{4\Delta}$ gives $\Omega/2\pi = 7.5 \pm 0.1\,\text{kHz}$ in perfect agreement with measurements via resonant Rabi flopping.

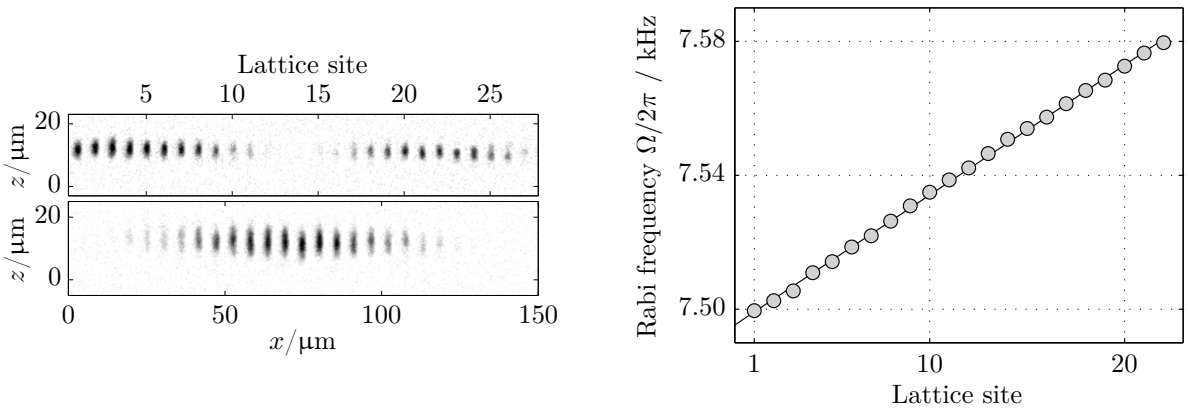

Figure 6: Microwave power gradient over the extent of the lattice. The **left** panel depicts a typical experimental picture obtained after 10 ms of resonant Rabi flopping between $|2,0\rangle$ (upper picture) and $|1,0\rangle$ (lower picture). The **right** panel shows that the Rabi frequency Ω varies linearly with lattice site. The gradient is 3.88 Hz/Well which amounts to 1.4 % from the very left to the very right of the cloud. This relative power gradient is due to geometry and independent of the absolute power used.

spreading eventually stops when a one-dimensional lattice is ramped up, trapping the atoms in the anti-nodes, distant by $\lambda_l \approx 5.5\,\mu\text{m}$. This situation is depicted in Figure 2.

At an initial magnetic field of $B \approx 9\,\text{G}$, we transfer the atoms in state $|1,-1\rangle$ to $|1,0\rangle$ by means of a radio-frequency π-pulse. At this magnetic field the second order Zeeman-effect is already high enough to ensure no significant population of the state $|1,1\rangle$. The magnetic field is subsequently ramped down to $B \approx 3\,\text{G}$. At this point a strong magnetic field gradient serves as a Stern-Gerlach cleaning pulse to remove all spurious atoms in both the $|1,-1\rangle$ state as well as the $|1,+1\rangle$ state. We are then left with a pure $m_F = 0$ condensate and raise the standing wave further to ensure the validity of the single-spatial-mode approximation, while at the same time reducing the magnetic field to the final value at which the experiment is performed.

The magnetic field is actively stabilized by means of a fluxgate sensor. The shot-to-shot fluctuations are less than $100\,\mu\text{G}$ at magnetic fields in the range of $B \approx 1\,\text{G}$. These remaining fluctuations play no role for the dynamics and the residual level fluctuations, $\delta E = 2qB\delta B \approx 140\,\text{mHz/mG}$ can be neglected. The same is true for the magnetic field gradient over the lattice, which is of the same order of magnitude as depicted in Figure 4.

Most of the experiments were performed at either $B = 1.64\,\text{G}$ or $B = 0.91\,\text{G}$. To compensate for the quadratic Zeeman effect and mean-field shift we chose $\Omega/2\pi = 7.56\,\text{kHz}(5.47\,\text{kHz})$ and $\Delta/2\pi = 100\,\text{kHz}(190\,\text{kHz})$ for $B = 1.64\,\text{G}(0.91\,\text{G})$. In both cases, we see no evidence for level shifts due to other couplings, e.g. the ones indicated by dashed, grey arrows in the left panel of Figure 5.

2 Spin-exchange as beam splitter

Now we have the experimental tools at hand to tailor the spin-exchange Hamiltonian such that it constitutes a well isolated non-linear beam splitter. This non-linear beam splitter will provide the basis of the SU(1,1) interferometer. In this section we study its effect in detail.

2.1 Non-linear amplification

The Hamiltonian $\mathcal{H}_{\text{inel}} = (c_2 - c_0)N_0 a_\downarrow^\dagger a_\uparrow^\dagger + \text{h.c.}$ constitutes a parametric amplifier [14, 15]. Its action has extensively been studied in Quantum optics [34–36].

2.1.1 SU(1,1) mode transformation

As an amplifier its effect can be described by a Bogoliubov mode transformation on the operators $a_\downarrow$ and $a_\uparrow$, mixing annihilation and creation operators [37]. The general transformation has the form [36]

$$\begin{pmatrix} a_\uparrow \\ a_\downarrow^\dagger \end{pmatrix} = \begin{pmatrix} \alpha & \beta \\ \gamma & \delta \end{pmatrix} \begin{pmatrix} a'_\uparrow \\ a'^\dagger_\downarrow \end{pmatrix} \tag{6}$$

The transformation is required to maintain the bosonic nature of the modes, viz $[a_{\uparrow(\downarrow)}, a^\dagger_{\uparrow(\downarrow)}] = 1$. This enforces $\alpha = \delta^*$, $\beta = \gamma^*$ and $|\alpha|^2 - |\beta|^2 = 1$ (unit determinant). A possible parametrization reads

$$\begin{pmatrix} a_\uparrow \\ a_\downarrow^\dagger \end{pmatrix} = \begin{pmatrix} \cosh r & e^{\mathrm{i}\varphi} \sinh r \\ e^{-\mathrm{i}\varphi} \sinh r & \cosh r \end{pmatrix} \begin{pmatrix} a'_\uparrow \\ a'^\dagger_\downarrow \end{pmatrix} = U(\varphi) \begin{pmatrix} a'_\uparrow \\ a'^\dagger_\downarrow \end{pmatrix} \tag{7}$$

As it turns out [8], φ can be controlled by changing the phase of the pump mode. This pump mode is assumed to be in a strong coherent field, such that it is not affected by removing atoms. Then the transformation only acts on the operators of the side modes. The parameter r is proportional to the evolution time t_{evo} and nonlinearity of the process, $r = (c_2 - c_0)N_0 t_{\text{evo}}$. This mode transformation somewhat resembles a Lorentz-transformation [38, 39]. The matrix $U(\varphi)$ belongs to the group of SU(1,1), which for real matrix elements is isomorph to the group of Lorentz transformations in two dimensions.

A passive beam splitter as in the Mach-Zehnder interferometer is described by the symmetry group of SU(2), which requires the conservation of atom number (equivalent to a constant L^2). Since the transformation (7) only considers the side modes, it seemingly

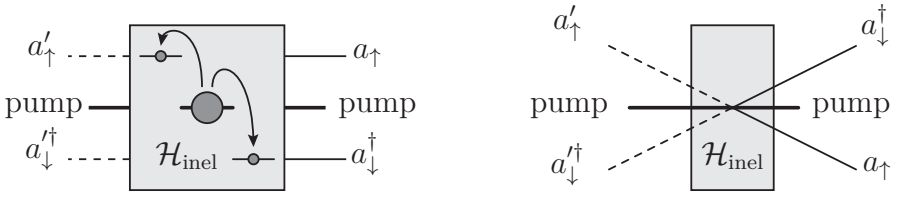

Figure 7: Mode-transformation on the operators performed by the Hamiltonian $\mathcal{H}_{\text{inel}}$. The Hamiltonian for spin-changing collisions (**left** hand side) is the same as for parametric down conversion in optics by means of non-linear crystals. We will use both representations interchangeably.

violates energy and particle conservation. Its action is described by a constant L_z rather than L^2. This means that the mean number of atoms in each side mode is identical, $\langle n \rangle = \langle a_\uparrow^\dagger a_\uparrow \rangle = \langle a_\downarrow^\dagger a_\downarrow \rangle$. It can easily be calculated to be

$$\langle n \rangle = \sinh^2 r \tag{8}$$

which describes exponential growth of the side mode population versus evolution time t_{evo}. The mode transformation can be rewritten in experimentally direct accessible quantities:

$$U(\varphi) = \begin{pmatrix} \sqrt{1+\langle n \rangle} & e^{\mathrm{i}\varphi}\sqrt{\langle n \rangle} \\ e^{-\mathrm{i}\varphi}\sqrt{\langle n \rangle} & \sqrt{1+\langle n \rangle} \end{pmatrix}$$

2.1.2 Experimental characterization

In Figure 9 (left panel) we study the exponential growth of the side mode population during spin-changing collisions: For short evolution times the experimental curve follows the theory expectation. For longer evolution times, however, further grow of the side modes eventually stops and the side mode population saturates. The onset of this can be seen for evolution times exceeding 280 ms where theory prediction and observed population clearly differ for the central lattice site (plot marker ◯).

This saturation is due to the break down of the low-depletion approximation: In the course of the parametric amplifier more and more atoms are removed from the pump mode and put into the side modes. Then the non-linearity $r \propto N_0$ decreases, which slows down the exponential growth. Additionally, the mean-field shift, given by the term $\mathcal{H}_{el}$ changes and creates an energy difference during the evolution time which translates into a phase mismatch. We can estimate this energy difference by requiring that a significant phase mismatch occurs at evolution times around 500 ms (at this point a peak side mode population is reached which for further times decreases again), $\Delta E t \approx 1/2$. Then the change of the mean-field shift amounts to $\Delta E = \mathcal{O}(1\,\mathrm{Hz})$. Thus already very small energy differences become relevant due to the long evolution time. A fact which will become important in the further discussion.

The exponent r describing the non-linearity is extracted for each lattice site individually in the right panel. It is expected to be proportional to the number of atoms N_0 in each particular site. As can be seen, this relation holds, but the proportionality factor is different for the centre and wings of the optical lattice. We attribute this to a power gradient of the microwave. The energy level shift due to microwave dressing varies over the extent of the optical lattice (see Figure 6) and perfect compensation of the quadratic Zeeman shift (and $\mathcal{H}_{\mathrm{el}}$) is not achieved everywhere, as can already be seen by naked eye in the raw data, Figure 8. Similarly to the case considered before this energy difference yields a phase mismatch which slows down the spin-exchange. A direct comparison of the spin-changing collisions for a central lattice site (◯) and one at the edge (□) is given in the left panel of Figure 9

Since the energy difference's origin is external it already affects the process in the very beginning, even when it is still in the low-depletion limit. To minimize this effect we changed the magnetic field from $B = 1.64\,\mathrm{G}$ to $B = 0.91\,\mathrm{G}$ and thereby reduced the quadratic Zeeman effect by a factor of three. To overcome this energy less power (only a third) is needed for microwave dressing, therefore reducing the inhomogeneity. The spin-changing collisions then take place over a wider range of lattice sites and more data can be collected.

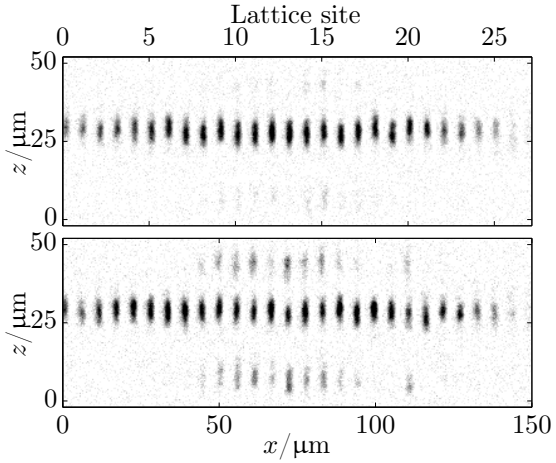

Figure 8: Typical experimental pictures of spin-changing collisions after an evolution time of 260 ms (upper panel) and 360 ms. A strong magnetic field gradient in z-direction serves as a Stern-Gerlach pulse to spatially separate the three m_F substates. The $|+1\rangle$ ($|-1\rangle$) state is torn upwards (downwards), while the $|0\rangle$ states experiences no force. The absorption imaging after about 1 ms time of flight is irrespective of the magnetic substate. Only atoms in the centre around lattice site 14 participate in the spin-exchange. A microwave power gradient over the cloud prevents the other lattice sites from being shifted into resonance, c.f. Figure 6

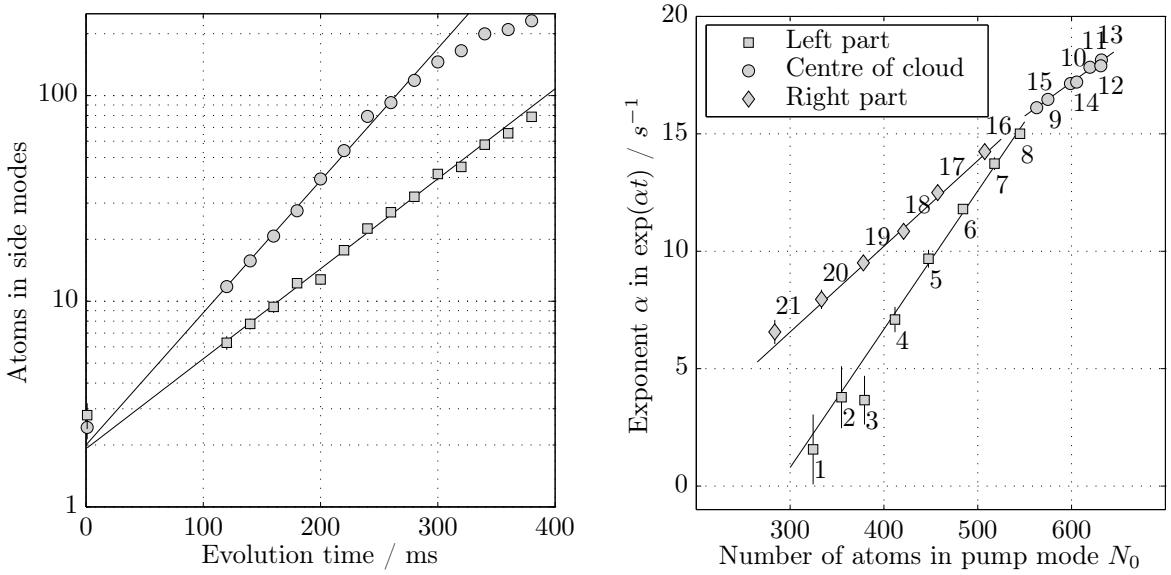

Figure 9: Dynamics of spin-changing collisions. **left)** For times up to $t_{\mathrm{evo}} \approx 250$ ms we observe no deviation from an exponential growth of the side mode atoms as expected from theory. However the exponent, describing the growth shows a spatial dependence. Besides the spatial dependence due to a microwave power gradient the proportionality to the pump mode atom number N_0 still holds as shown in the **right)** panel. The numbers indicate which specific lattice site (for a definition, c.f. Figure 8) has been analyzed.

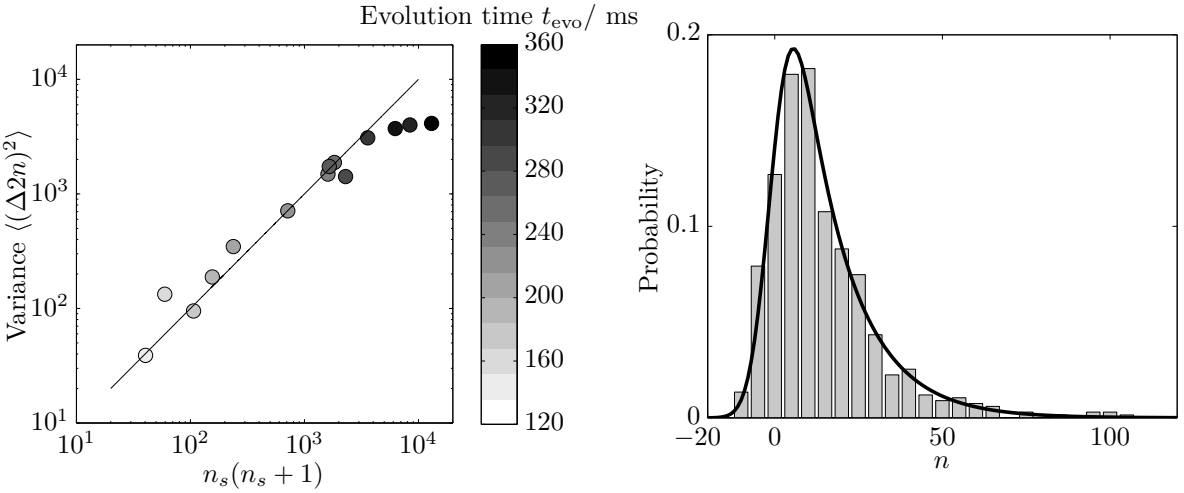

Figure 10: The spin-changing collisions produce a state which is highly fluctuating in atom number. **Left)** Variance versus mean atom number inside the interferometer for different evolution times. The line shows the theory prediction, $\langle(\Delta 2n)^2\rangle = n_s(n_s+1)$, where $n_s = 2\langle n\rangle$ Deviations become apparent only for evolution times larger than 280 ms. **Right)** Histogram of observed side mode population n after spin-changing collisions for 160 ms. The black line is a fit to theory (thermal state, equation (10)) also taking into account detection noise by convolution with a Gaussian. The detection noise is $\sigma = 5.5$ atoms and has been determined independently.

2.2 Generation of entanglement

By exploiting quantum effects such as entanglement the standard quantum limit can be surpassed [5, 40].

2.2.1 Two-mode squeezed vacuum and twin-atom states

The parametric amplifier entangles the two side modes, leaving their atom number difference constant. The quantum state after the spin-changing collisions is given by [34]:

$$|\Psi\rangle = \frac{1}{\tanh r}\sum_n e^{in\varphi}\tanh^n r\,|n\rangle_\uparrow\,|n\rangle_\downarrow \tag{9}$$

where $|n\rangle_{\uparrow(\downarrow)}$ denotes the Fock state with exactly n atoms in mode $|+1\rangle$ ($|-1\rangle$), which also constitute the Schmidt-basis in this case. Since there are infinitely many Schmidt coefficients this is a highly entangled state also known as two-mode squeezed vacuum [41, 42]

2.2.2 Looking at a single mode

From the Schmidt decomposition follows that tracing out one mode leaves the other mode $|n\rangle$ in a mixed state described by the density matrix

$$\rho = \frac{1}{\tanh^2 r}\sum_n \tanh^{2n} r\,|n\rangle\langle n| = \sum_n \frac{\langle n\rangle^n}{(1+\langle n\rangle)^{n+1}}\,|n\rangle\langle n| \tag{10}$$

This density matrix describes a thermal state with mean atom number $\langle n\rangle = \sinh^2 r$ and variance $\langle(\Delta n)^2\rangle = \langle n\rangle(\langle n\rangle + 1)$. In Figure 10 we compare these expectations to experimental results and show that they hold very well for not too long evolution times.

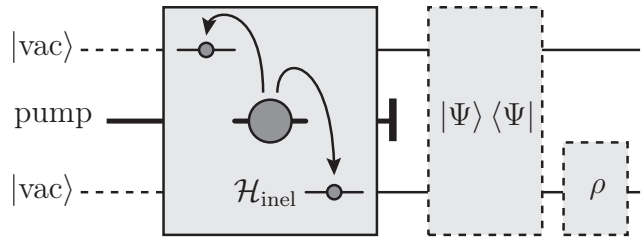

Figure 11: Entanglement. The spin-exchange produces the perfectly correlated state $|\Psi\rangle$, called two-mode squeezed vacuum. While the entire system is in a pure state $|\Psi\rangle\langle\Psi|$ and consequently bears no entropy, its individual modes are in a thermal and thus mixed states described by a density matrix ρ, equation (10). This is the hallmark of entanglement.

3 SU(1,1) interferometer

Substituting the beam splitters of a Mach-Zehnder interferometer with parametric amplifiers yields the so-called SU(1,1) Interferometer as depicted in Figure 12.

It has been shown theoretically that in such an interferometer the phase difference φ_s accumulated between the upper and lower arm can be estimated at the Heisenberg limit. The number of atoms n_s sensing the phase shift φ_s is given by the average number of atoms in both side-modes, $n_s = 2\langle n \rangle$. The Heisenberg-limit therefore reads $\langle (\Delta\varphi_s)^2 \rangle = \mathcal{O}(1/n_s^2)$.

3.1 Working principle: Undoing spin-changing collisions

For an individual parametric amplifier the pump mode merely provides the necessary energy and particle resources for amplification of the initially empty side-modes. In this setup, however, the pump mode plays a more involved role. Changing the phase of the pump mode in between both parametric amplifiers sets the second process to reverse the effect of the first one.

Even a small differential phase accrued by only few atoms in the side-modes foils the reversibility and leaves the output state different from the otherwise perfectly reconstructed input vacuum state. It is this increased vulnerability for phase mismatches of the second non-linear process which yields Heisenberg limited phase sensitivity. Unfortunately, this implies that enhanced phase estimation only works around $\varphi_s = 0$. To overcome this drawback one can in principle introduce an additional, known phase shift into the other arm until the differential phase shift is balanced, thereby implementing a feed-back on the interferometer's set-point [8].

3.1.1 Experimental control over the pump phase

The key idea of the SU(1,1) interferometer is to reverse the dynamics of the second parametric amplifier. This is done by introducing a phase shift of $\pi/2$ into the otherwise common pump mode, amounting to the change $a_0 \to \mathrm{i}a_0$. The Hamiltonian $\mathcal{H}_{\mathrm{inel}} \propto a_0^\dagger a_0^\dagger a_\uparrow a_\downarrow + \mathrm{h.c.}$ changes sign under this transformation which means that time evolution is reversed: $U(t) = e^{\mathrm{i}\mathcal{H}t} \to e^{\mathrm{i}\mathcal{H}(-t)} = U(-t)$.

By turning off the microwave dressing, the second order Zeeman effect is not compensated and the conditions for the spin-exchange are not met any longer. Then the spin-changing collisions stop and the energy difference between the $|0\rangle$ and $|\pm 1\rangle$ modes yields a differential phase. This phase is given by $\varphi_0 = \Delta E t_{\mathrm{phase}}$, if t_{phase} is the duration

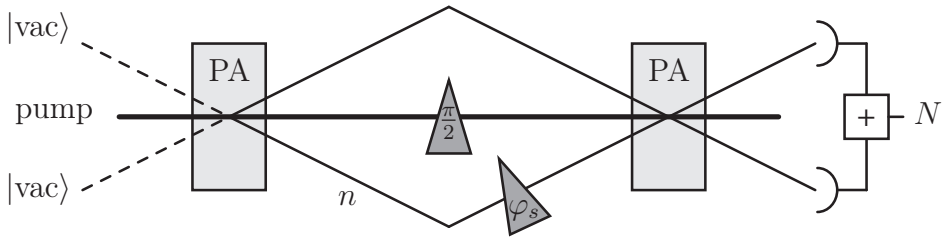

Figure 12: Setup of an SU(1,1) Interferometer. The beam splitters of a Mach-Zehnder interferometer are substituted by parametric amplifiers (PA). The second parametric amplifier is set to reverse the effect of the first by introducing a phase shift of $\pi/2$ in the pump mode. Heisenberg-limited performance is expected only around $\varphi_s = 0$.

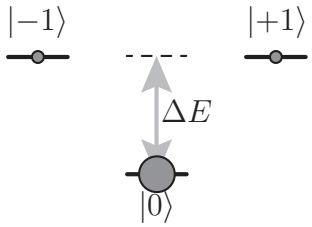

Figure 13: Experimental control over the pump-phase. Spin-exchange is initiated by dressing the $|0\rangle$ level to be energetically as high as the side-mode levels $|\pm1\rangle$. Once the dressing microwave is turned off the energy mismatch ΔE yields to a differential phase φ_0 building up versus time $t_{\rm phase}$ as $\varphi_0 = \Delta E t_{\rm phase}$. The energy difference is almost completely given by the second order Zeeman shift, $\Delta E = qB^2$, since the mean-field shift can be neglected in the low depletion limit.

where the energy difference ΔE is maintained. Since the mean-field shift can be neglected the energy difference ΔE is given by the second order Zeeman effect, $\Delta E = \mathcal{H}_{B^2} = qB^2$. The linear Zeeman effect is irrelevant due to the special superposition of $|+1\rangle$ and $|-1\rangle$ showing up in equation (9).

3.1.2 Which phase is actually being measured?

The first parametric amplifier produces the two-mode squeezed vacuum state $|\Psi\rangle$ of equation (9). The phase shift φ_s between both arms then shows up in all powers of $e^{\mathrm{i}\varphi_s}$, making it very distinct from the state $|\Psi\rangle$ already for small phase changes φ_s. Since the second parametric amplifier is set to undo the dynamics for state $|\Psi\rangle$ it fails so for non-zero phase shift φ_s. This is a very general concept and has already been applied to prove the entanglement production of particular processes in ion traps [43] and optics [44].

The entire SU(1,1) interferometer as shown in Figure 12 performs the transformation

$$\begin{pmatrix} a_\uparrow \\ a_\downarrow^\dagger \end{pmatrix} = U(\pi/2) \begin{pmatrix} 1 & 0 \\ 0 & e^{i\varphi_s} \end{pmatrix} U(0) \begin{pmatrix} a_\uparrow \\ a_\downarrow^\dagger \end{pmatrix}$$

However, from a mathematical point of view it is somewhat artificial to distinguish between the phase $\varphi_s = \varphi_\uparrow - \varphi_\downarrow$ with $\varphi_{\uparrow(\downarrow)}$ denoting the phase of mode $|+1\rangle$ ($|-1\rangle$), and the pump mode phase φ_0. This becomes obvious when considering the underlying Hamiltonian $\mathcal{H}_{\rm inel} \propto e^{\mathrm{i}\varphi} a_0 a_0 a_\downarrow^\dagger a_\uparrow^\dagger + \text{h.c.}$, where the only relevant phase which enters is given by $\varphi = (2\varphi_0 - \varphi_\uparrow - \varphi_\downarrow)$. Although conceptually quite different, the same interferometer is described by the much simpler transformation

$$\begin{pmatrix} a_\uparrow \\ a_\downarrow^\dagger \end{pmatrix} = U(\varphi) U(0) \begin{pmatrix} a_\uparrow \\ a_\downarrow^\dagger \end{pmatrix} \tag{11}$$

This transformation explicitly reads

$$a_\uparrow = \mu a_\uparrow + \nu a_\downarrow^\dagger \tag{12}$$

$$a_\downarrow = \nu a_\uparrow^\dagger + \mu a_\downarrow \tag{13}$$

with $\mu = n(1 + e^{\mathrm{i}\varphi}) + 1$ and $\nu = \sqrt{n(n+1)}(1 + e^{\mathrm{i}\varphi})$. For $\varphi = \pi$ we have $\mu = 1$ and $\nu = 0$, such that the initial vacuum is restored. Also $|\nu|^2 = 2n(n+1)(1 + \cos\varphi)$ and $|\mu|^2 = |\nu|^2 + 1$, as expected for an SU(1,1) transformation [45].

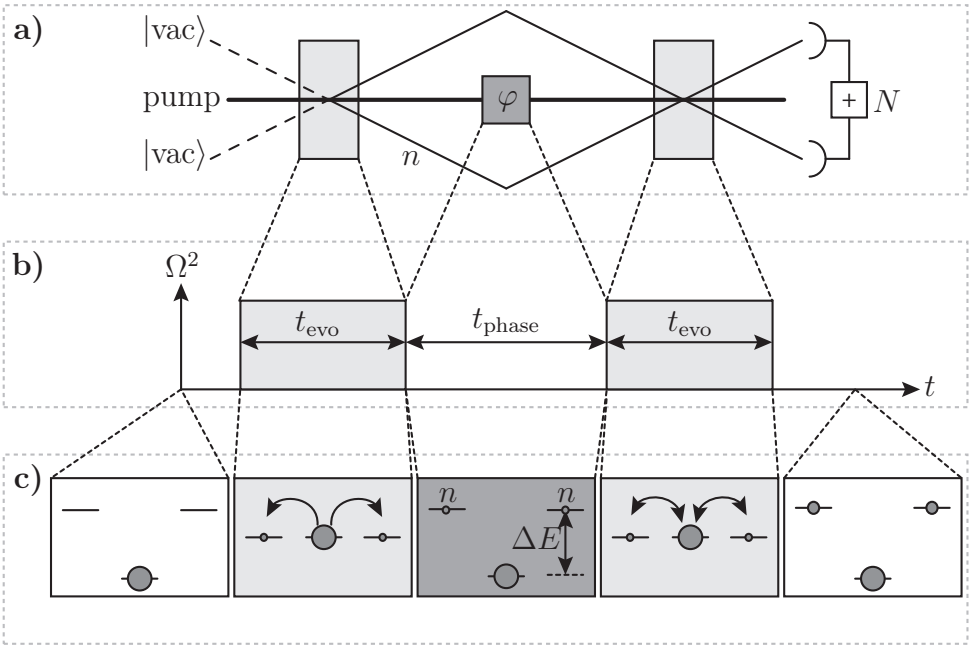

Figure 14: Experimental realization of the SU(1,1) interferometer. The upper panel **a)** shows the schematic adopted from the original optical proposal. Panel **b)** shows the timing diagram of the microwave power $\propto \Omega^2$ used for dressing. It is turned on for time t_{evo} to facilitate spin-changing collisions and turned off for time t_{phase} in between. Panel **c)** shows the involved energy levels. The Rabi frequency Ω used for microwave dressing is chosen such that it compensates the level shift due to the quadratic Zeeman effect. The phase φ builds up via the energy difference ΔE during time t_{phase} without compensating microwave, $\varphi = 2\Delta E t_{\mathrm{phase}}$. The number of atoms inside the interferometer is $2n$. This number gets non-linearly amplified by a second period of spin-changing collisions and the atom number N is measured in the end.

3.1.3 Experimental realization

Since we have direct experimental control over the pump phase φ_0, the transformation (11) can directly be implemented as depicted in Figure 14. The interpretation, however, changes slightly: In its original proposal the interferometer directly resembles the Mach-Zehnder interferometer since it had only two arms and measures its relative phase difference φ_s. It is then intuitively clear that the phase sensing atoms are those in the sidearms while those in the pump mode just ensure functionality but do not intervene otherwise.

In this configuration, however, the phase of the pump mode is scanned and the output signal is recorded. Still the side-mode population of just a few atoms influences the observed fringe and we can use this setup nonetheless to measure the phase shift experienced by atoms in the side-mode. This is similar to what [8] mentioned by a feedback, i.e. to introduce a known phase shift into the other arm to shift the interferometer's working point to its maximal sensitivity. We do not shift one of the interferometer arms in phase to level the differential phase however, but instead introduce a known phase shift into the pump mode.

3.2 Observed interferometry fringe

The output signal of the interferometer is given by the mean number of atoms in the side-modes $\langle N \rangle$, see Figure 14. This is different from the usual SU(2) Mach-Zehnder interferometer where the *total* number of atoms is conserved (this corresponds to L^2) and read-out is given by the operator L_z, viz the atom number *difference* after the last beam splitter. For the SU(1,1) interferometer the situation is interchanged, since L_z remains constant. The phase dependent output is then given by

$$\langle N \rangle = \langle a_\uparrow^\dagger a_\uparrow \rangle + \langle a_\downarrow^\dagger a_\downarrow \rangle = 2|\nu|^2 = n_\mathrm{s}(n_\mathrm{s}+2)(1+\cos\varphi) \tag{14}$$

where $n_\mathrm{s} = 2\langle n \rangle$ is the phase sensing mean atom number inside the interferometer. Due to the non-linear amplification already very small side-mode populations (as low as a few atoms on average) inside the interferometer translate into a phase-dependent output.

3.2.1 Importance of a non-depleted pump mode

In Figure 15 we show an experimentally obtained fringe for different evolution times of the parametric amplifier. In any case, the duration of spin-changing collisions is always the same for both parametric amplifiers. The ideal theory assumes no pump-depletion whatsoever and an infinitely large pump mode, allowing the state inside the interferometer to be a coherent sum of infinitely many twin Fock states. As already seen in Figure 10 deviations from theory arise for evolution times exceeding 250 ms. In the SU(1,1) interferometer reversibility gets degraded the longer the evolution time and a phase-independent atom number offset appears. At phase time $t_\mathrm{phase} \approx 1.8\,\mathrm{ms}$ a phase of $\varphi = \pi$ is accumulated. Via the relation $\varphi = 2\varphi_0 = 2\Delta E t_\mathrm{phase}$ we can estimate the ΔE to be given by the second order Zeeman shift exclusively. At this stage we observe no difference in frequency for different side-mode populations, indicating an unobservable small mean-field shift as already taken for granted before.

3.2.2 Frequency of phase evolution

The frequency of the observed fringe is given by the energy difference during the phase time in between both parametric amplifiers. To check this for a wider energy range, we applied microwave dressing also during the time t_phase such that the energy difference could be varied by changing the microwave detuning Δ to resonance $|1,0\rangle \leftrightarrow |2,0\rangle$. In Figure 16 we show the observed fringe frequencies, extracted from measurements similar to those shown in Figure 18, including four full periods of the fringe. The observed frequencies follow the expected law for microwave dressing, equation (5), and the fitted slope agrees well with independent measurements of the resonant Rabi frequency Ω.

3.3 Sensitivity

The SU(1,1) interferometer has especially been discussed in the context of improved phase sensitivity.

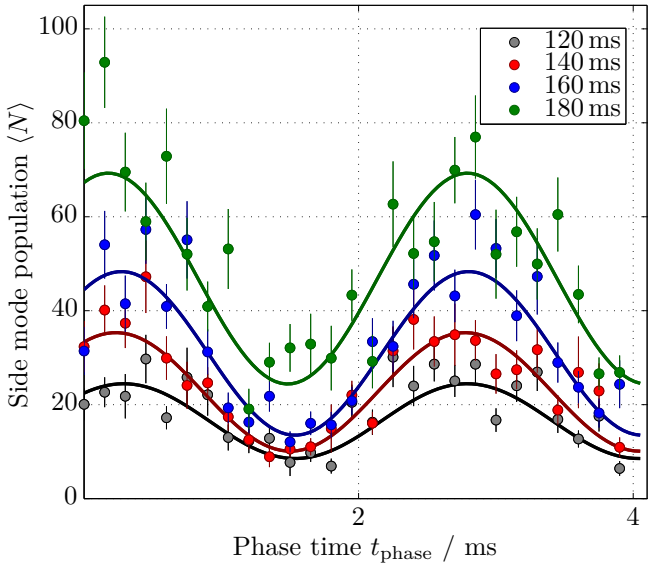

Figure 15: Interferometer fringe for different evolution times. For longer evolution times reversibility is diminished and a phase independent atom offset appears. Five adjacent wells have been averaged for increased statistics without any atom number post-selection. The frequency of each fringe is about 390 Hz consistent with an energy difference exclusively due to the second order Zeeman effect at magnetic field $B = 1.64\,\mathrm{G}$.

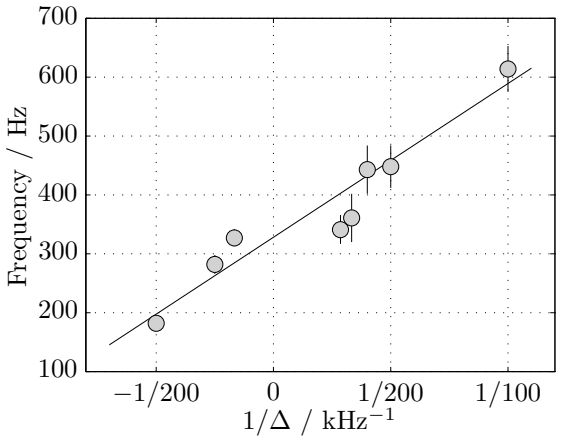

Figure 16: Frequency of the output fringe. During phase evolution microwave dressing is usually turned off and the frequency of the fringe is given by twice the energy difference due to the quadratic Zeeman effect. Here we additionally dress the $|0\rangle$ mode during phase evolution to address various energy differences. The observed fringe frequency is in accordance with the theoretical expectation: The fit to the data gives a $\Omega/2\pi = 7.2 \pm 0.5\,\mathrm{kHz}$, which agrees with independent measurements via resonant Rabi flopping. For no additional microwave dressing, i.e. the scenario in which the fringe of Figure 15 has been recorded, the fit predicts a frequency of $f = 267 \ldots 389\,\mathrm{Hz}$ compliant with our experimental observation.

3.3.1 Theory

The sensitivity $\langle(\Delta\varphi)^2\rangle$ of the interferometer can be calculated via error propagation [8, 45],

$$\langle(\Delta\varphi)^2\rangle = \langle(\Delta N)^2\rangle \Big/ \left|\frac{\partial\langle N\rangle}{\partial\varphi}\right|^2 \tag{15}$$

and thus depends on both, the variance $\langle(\Delta N)^2\rangle$ of the output signal $\langle N\rangle$ as well as its rate of change with parameter φ.

Inserting

$$\frac{\partial\langle N\rangle}{\partial\varphi} = n_\mathrm{s}(n_\mathrm{s}+2)\sin\varphi \tag{16}$$

and

$$\begin{aligned}\langle(\Delta N)^2\rangle &= 4|\nu|^2|\mu|^2 = n_\mathrm{s}(n_\mathrm{s}+2)(1+\cos\varphi)\left[2+n_\mathrm{s}(n_\mathrm{s}+2)(1+\cos\varphi)\right]\\ &= 2n_\mathrm{s}(n_\mathrm{s}+2)(1+\cos\varphi)+\left[n_\mathrm{s}(n_\mathrm{s}+2)(1+\cos\varphi)\right]^2\end{aligned} \tag{17}$$

yields

$$\langle(\Delta\varphi)^2\rangle = \frac{1}{1-\cos\varphi}\left[\frac{2}{n_s(n_s+2)}+(1+\cos\varphi)\right] \tag{18}$$

which proves that Heisenberg scaling is achieved. The Heisenberg limit itself is attained for large mean atom number n_s and only around $\varphi=\pi$, as long as the second term in square brackets does not start to dominate [45]. For small mean atom number n_s performance around $\varphi=\pi$ is even better than the Heisenberg-limit. The SU(1,1) interferometer thereby constitutes a somewhat counter intuitive example of increased phase sensitivity around a fringe minimum, i.e. a dark fringe. At this working point the derivative vanishes and the sensitivity comprises a division of zero by zero. This makes the observable sensitivity very susceptible towards excess noise. Figure 17 shows the expected sensitivity for $n_s = 2.5$ atoms on average inside the interferometer in the ideal case (dashed grey line) and also with excess detection noise of $\sigma = 1$ atom (black line). The right panel shows the range of phases φ for which Heisenberg-limited performance is expected versus the number of atoms n_s inside the interferometer. This has been estimated by requiring $1+\cos\varphi < 2/n_s(n_s+2)$ as in [45].

In [45] the performance of the SU(1,1) interferometer is studied taking losses into account: While the absence of internal loss is indispensable, perfect detection is not so crucial. Detection inefficiencies only affect the reached phase precision by a factor, i.e. the Heisenberg limit might not be reached, but does not prevent one from still observing Heisenberg scaling.

The improved sensitivity stems from the fact that signal and variance have different functional dependencies. While the signal $\langle N\rangle$ varies like a cosine, the variance additionally involves a higher Fourier component, see equation (17). This yields a significantly flatter behaviour at the minimum, as can be seen in the right panel of Figure 18.

3.3.2 Experimental extraction of the phase sensitivity

To stay within the low-depletion limit we perform spin-changing collisions for 80 ms. In Figure 19 a) we show the recorded output fringe which comprises about half a period in order to be able to fit a cosine. From the amplitude of this fit we can extract the mean

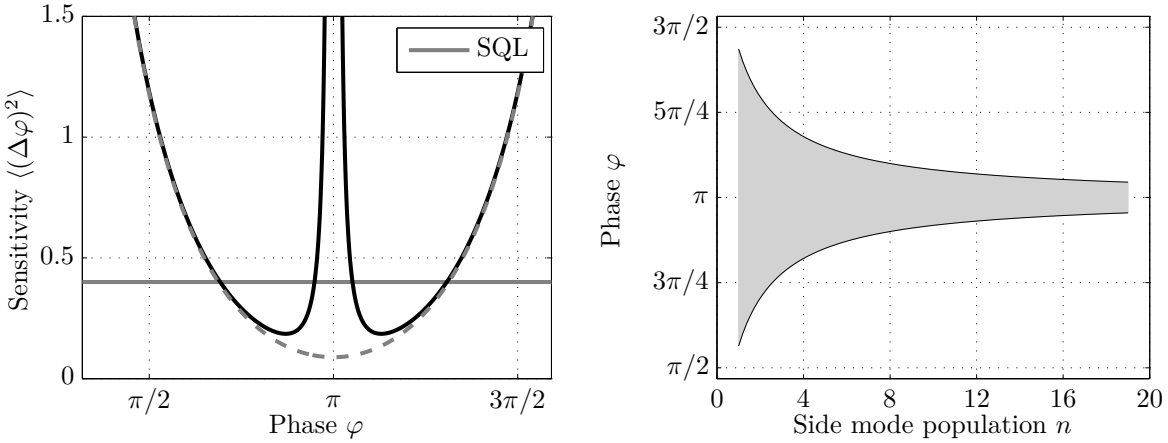

Figure 17: Left) Effect of detection noise on the sensitivity of the SU(1,1) interferometer. The sensitivity is given by error propagation and thus by the quotient of obtained variance and the derivative of the output signal as detailed in the text. In theory a division of zero by zero is encountered at phase $\varphi = \pi$, which gives a defined result. Due to finite detection noise, however, the observed variance is never excactly zero and a singularity arises due to the division by essentially zero. **Right)** Heisenberg limited performance is only expected around $\varphi = \pi$. The range of phases φ for which this sensitivity is reached shrinks for greater side-mode population as given by equation (18)

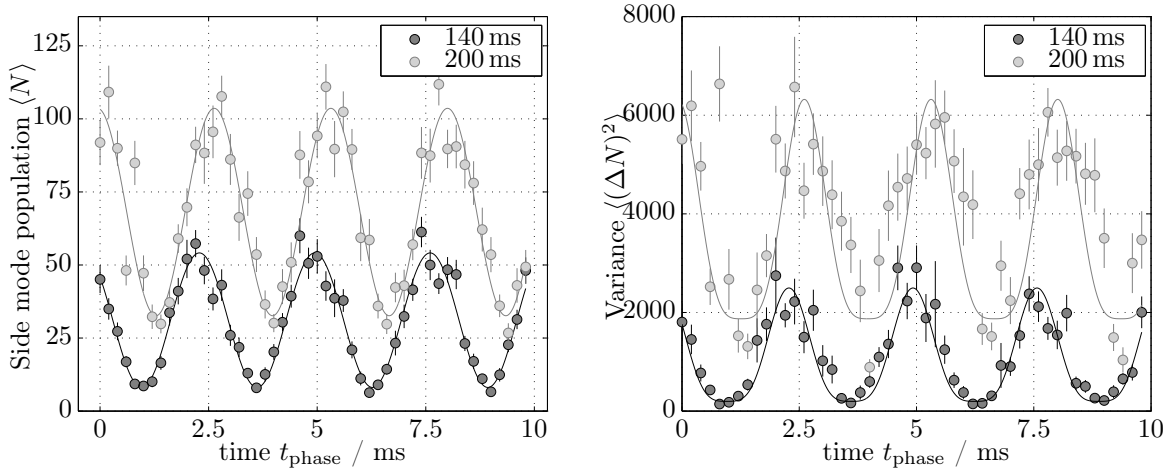

Figure 18: Left) SU(1,1) interferometer fringe for two experimental runs with different evolution times of the beam splitters. The line is a fit to equation (14) with an additional phase-offset, which will be discussed in Section 3.4. According to the fit, the mean number of atoms inside the interferometer is $n_s = 3.9 \pm 0.1$ or $n_s = 5.0 \pm 0.2$, respectively. Although the mean number of atoms differs by only one atom, the two curves can clearly be distinguished. **Right)** Observed variance. Error bars have been estimated by a jackknife procedure, as detailed in the text. The line is a fit to equation (17). The observed variance for 140 ms of spin-changing collisions in each beam splitter fits better to the theoretical expectation than the 200 ms one. The flattened behaviour around its minima is a characteristic of the SU(1,1) interferometer. Fits of the output signal (**left**) as well as fits of the output variance (**right**) yield identical values on the mean atom number inside the interferometer.

atom number inside the interferometer which is $n_s = 2.5 \pm 0.2$ atoms, see equation (14). Even for this small atom number complete reversibility is not achieved at phase $\varphi = \pi$. Additionally, imperfections of the absorption imaging lead to an atom-independent offset of about two atoms as indicated by the dashed line.

To properly account for detection inefficiencies we performed the same experimental sequence without spin-changing collisions such that the side-modes are left empty. These measurements are taken interleaved with the actual SU(1,1) interferometer to also contain eventual drifts during the experiment. In Figure 20 we show histograms of the observed atom number for both empty modes $|\pm 1\rangle$. The mean atom number clearly differs from zero and is, furthermore, different in the two regions. This is most likely due to problems with stray light which we will resolve in future experiments.

More important than the mean atom number is the variance, which is mainly given by photon shot-noise of the laser beam used for absorption imaging [17]. Phase estimation is expected to perform best at a fringe minimum where the derivative vanishes and a division by zero is encountered. This makes it extremely sensitive to any excess noise. We thus rely on the subtraction of detection noise, which we find to have a Gaussian distribution and is characterized by its Gaussian width σ.

In Figure 19 b) the resulting detection noise is indicated by the dashed line. While the variance roughly resembles the squared mean signal it is much flatter in its minimum, i.e. around phase π. This is expected from theory, equation (17), since the variance includes a second Fourier component. The black line is a fit to the theory prediction and fits the data very well. For comparison we also show a cosine fit in grey. Most strikingly it goes below the value of mere detection-noise, which is unphysical. This is shown in more detail in panel c). The variance includes about 90 experimental realizations in the same lattice site. The fit predicts a mean number of atoms inside the interferometer of $n_s = 2.8 \pm 0.2$ atoms consistent with the results obtained from the mean atom number $|N\rangle$ in panel a). Error bars of the variance are obtained by a jackknife procedure: Here, the error is estimated by calculating the variance for an ensemble containing all data points but one. One excludes each data point exactly once and calculates the variance for the remaining ones. Since this is based on resampling, statistically dependent results are obtained which nevertheless give an accurate estimate of the error [46].

In panel d) the sensitivity is plotted. The thick black line gives the shot-noise limit $\langle(\Delta\varphi)^2\rangle = 1/n_s$ for the average atom number $n_s = 2.5$ atoms obtained from the fringe in panel a). To not overestimate the fringe's derivative, the fit allows for a constant atom offset. The error bars take into account both uncertainties in the variance as well as fit errors of the observed output fringe. Due to the limited number of measurements the statistical error of the variance is most important in this case. However, we also include the fit uncertainties of the detection noise. The thin black line is a fit of the theoretically expected performance, equation (18). The fit yields a mean atom number of $n_s = 1.5 \pm 0.2$ significantly lower than what we expect. Data points in direct proximity to the minimum at $\varphi = \pi$ have been excluded since a division by essentially zero makes them extremely vulnerable to excess noise. The dashed line gives the theory prediction for $n_s = 2.5$ atoms. The error bars are too large to make any quantitative statement yet.

3.4 Challenges and opportunities in an optical lattice

The one-dimensional optical lattice allows in principle to perform the experiment in all lattice sites in parallel and independent of each other. However, due to spatial

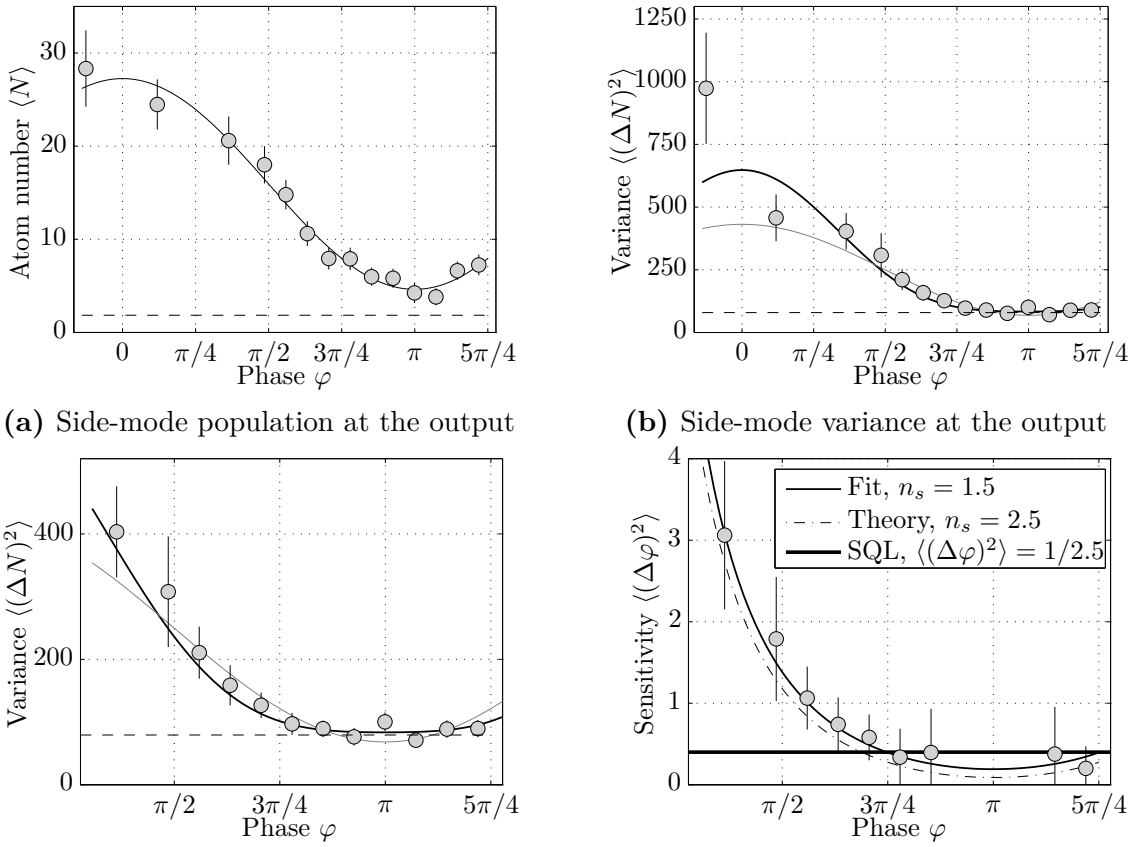

(a) Side-mode population at the output

(b) Side-mode variance at the output

(c) Zoom-in of panel b)

(d) phase-sensitivity around $\varphi = \pi$

Figure 19: Measured phase sensitivity for an evolution time of 80 ms at magnetic field $B = 0.91$ G. Panel a) shows the output fringe. The dashed line indicates an atom offset due to imperfect detection, which has been determined independently. Still reversibility at phase π is not reached. From the sinusoidal fit of panel a) a mean atom number of $n_s = 2.5$ is expected to be inside the interferometer. Panel b) shows the variance $\langle(\Delta N)^2\rangle$. The dashed line indicates detection noise, mainly due to photon shot-noise. The black line is a fit to equation (17) including two Fourier components, while the grey line indicates a cosine, unphysically going below the detection noise. c) is a zoom-in of the variance in the vicinity of the minimum, $\varphi = \pi$, illustrating the flattened behaviour. Panel d) shows the obtained sensitivity. A fit to equation (18) predicts a mean atom number of $n_s = 1.5$ and thus a reduced sensitivity compared to $n_s = 2.5$. However, both curves are within the error bars (1σ). We post-selected experimental realizations with total atom number in the range 630 ± 20 atoms.

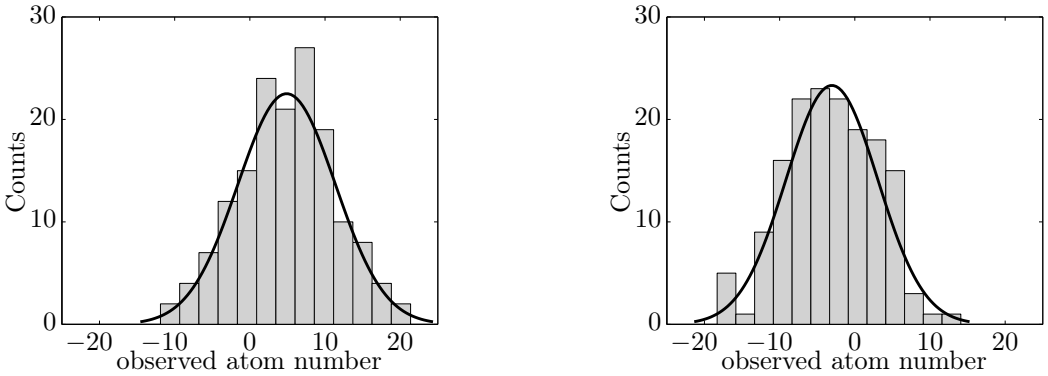

Figure 20: To characterize the detection noise of the absorption imaging we routinely perform experiments without atoms in the side-modes. These measurements are taken interleaved with the SU(1,1) interferometer. Due to technical imperfections we observe a small atom number offset. The left (right) histogram shows the obtained atom numbers for the $|+1\rangle$ ($|-1\rangle$) state. The mean atom number, $\mu = 4.9$ or $\mu = -3$, respectively, is clearly different from zero. The width of the Gaussian fit is $\sigma = 6.5 \pm 0.4$ atoms in the left histogram and $\sigma = 6.1 \pm 0.4$ atoms in the right one.

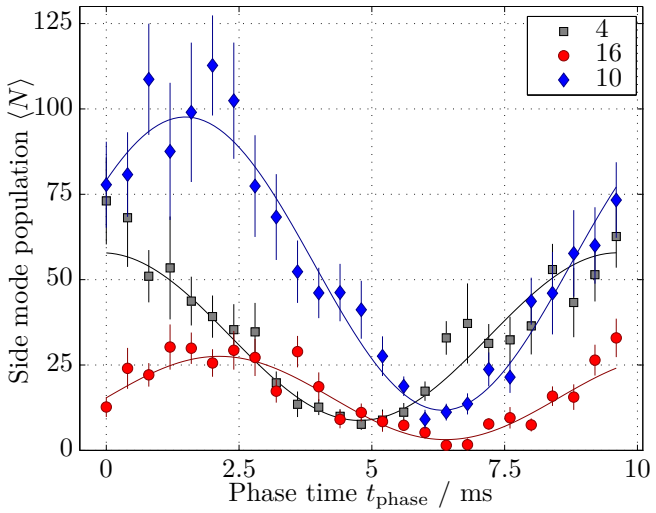

Figure 21: Many Realizations in an optical lattice. Shown is the mean side mode population $\langle N \rangle$ of the SU(1,1) interferometer for different phase times. As already expected from Figure 9 the amplitude shows a spatial dependence, inherited from the two constituent periods of spin-changing collisions ($t_{\mathrm{evo}} = 155\,\mathrm{ms}$). However not only does the amplitude vary with lattice position, so does the phase. The legend states which particular lattice site has been analyzed.

inhomogeneities each well looks markedly different. We demonstrate this in Figure 21, showing the output fringe for different lattice sites at a magnetic field of $B = 0.91\,\mathrm{G}$. Both the amplitude and the phase of the observed fringes differ from lattice site to lattice site. The reduced amplitude for sites at the edge of the lattice can be understood easily and is inherited from the spatial dependence of the spin-changing collisions, c.f. Figure 9. Since the amplitude represents the number of atoms inside the interferometer, each lattice site probes the sensitivity for different n_s. One of the appealing features is that the atom number scaling of the sensitivity might thus be measured in parallel. In this perspective the spatial inhomogeneity might come as a handy feature.

What is more perturbing is the different starting phase of the fringe for different lattice sites. We attribute this to the failing of the approximation of well separated individual processes, i.e. an isolated beam splitter at a time and only after that phase evolution. In reality, phase evolution occurs also during the beam splitter period, as already noted in section 2.1.2. When discussing the spin-changing collisions we saw that the phase evolution due to energy mismatches limits the growth of the side modes. Now we can directly observe this phase mismatch as the starting phase of the fringe. Moreover we can separate both contributions: The change of the mean-field shift and the power gradient of the microwave dressing.

The power gradient shows up when comparing neighbouring lattice sites. In the ideal theory the mean atom number is given by a cosine. In Figure 22 (right panel) we plot the starting phase of the fringe versus lattice position for an evolution time of 140 ms. In the ideal case the phase of the cosine is zero. A phase $\varphi > 0$ denotes an already evolved fringe, as described by $\cos(\omega t_{\mathrm{phase}} + \varphi)$.

Qualitatively the microwave dressing yields an overcompensation, i.e. the pump mode is energetically higher than the side modes, for the right part of the lattice. In the left part the pump mode is energetically *lower* than the side modes. After the first period of spin-changing collisions, that is during the time left for phase evolution t_{phase}, the pump mode is also shifted *down* in energy. One therefore expects, that the overall observed phase is greater in the left part of the cloud. This resembles what we observe in Figure 22 (right panel).

The linear dependence of the phase over lattice position is evident. The magnitude of the slope can be made plausible by a simple estimation: The microwave power gradient amounts to a change of Rabi frequency by $\delta\Omega/2\pi = 3.9\,\mathrm{Hz}$ per lattice site. This translates into a energy level shift of about $\delta E = 0.15\,\mathrm{Hz}$ per lattice site. A rough estimate for the phase shift would thus read $\delta\varphi = 2\pi\delta E t_{\mathrm{evo}} \approx \frac{\pi}{2}$ for 10 lattice sites. This is very similar to what we observe experimentally.

It is remarkable that at the point where the spin-changing collisions work best, i.e. lattice site 13, c.f. Figure 22, a non-zero phase shift of $\approx \pi/4$ is accrued. We believe that this is due to the changing mean-field shift: The phase is positive, which means that the pump mode is energetically lower than the side modes and phase already runs ahead. This is consistent with a mean field shift interpretation: In the course of the spin-changing collisions atoms are removed from the pump which is why the pump-level shifts down in energy.

We checked whether or not the same holds for longer evolution times. We still find a linear dependence of the phase with lattice site, but the deviations between the observed slope and our simple estimation are more severe. This might be due to the larger contribution of mean-field shifts for longer evolution times. In particular, it might not be possible to separate between the microwave gradient and the mean-field shift as looking at

the slope and offset separately.

3.4.1 Assessing technical limitations

Since heavy fluctuations are inherent to the spin-changing collisions one needs many experimental repetitions to extract mean values and variances. Long-term stability is thus of utmost importance. The spin-exchange relies on both a stable magnetic field as well as reliable microwave dressing.

We routinely perform Ramsey-type experiments on magnetically sensitive states to adjust the set point of the electronic feedback loop regulating the magnetic field. This is necessary since the sensitivity of the magnetic field sensor reacts on slow temperature drifts. These measurements are interleaved with those of the actual SU(1,1) interferometer. Long term fluctuations are lower than $\delta B = 0.5\,\mathrm{mG}$ and can be considered irrelevant for the spin-exchange.

The spin-changing collisions are most sensitive to long-term drifts of the microwave power. Due to the microwave gradient power fluctuations show up as the wandering around of resonant spin-exchange in the optical lattice: Then the lattice sites participating in spin-exchange change. For instance if we start with resonant spin-exchange in the centre it drifts to one edge of the lattice. All experiments are typically performed during an entire weekend to collect sufficient data and to minimize external influences. Usually, long term drifts are due to temperature fluctuations. Although the lab's temperature is actively stabilized, residual changes lead to a varying microwave power of about 1% over the course of a weekend, which directly show up in the experimental pictures.

The one-dimensional optical lattice helps us to assess the consequences of long term drifts of this type: The overall drift has a similar magnitude as the microwave power gradient when applied over the entire lattice. In the preceding paragraph we explained why each lattice site looks distinct. In particular the varying starting phase of the output fringe is bothering. A fluctuating microwave power yields the same phase jitter but in time instead of lattice site. This might be the reason why we did not observe sub-shot noise performance so far. For higher side mode population inside the interferometer the phase jitter becomes even more important, since theory predicts that Heisenberg limited phase estimation is only possible within a small range around phase $\varphi = \pi$, see Figure 17. To check this we built in a microwave power stabilization and are now repeating the SU(1,1) experiments. First results for the sensitivity look promising and are presented in the following section.

3.5 Preliminary results with revised microwave dressing

In Figure 23 we show the results of an experiment very much like the one discussed in Section 3.3.2, but now with revised microwave power stabilization. In direct comparison to the result obtained before we find a much higher mean atom number n_s inside the interferometer. In both experiments we only considered central lattice sites, in which spin-exchange worked best and averaged a single lattice site over a weekend of measurements.

A fit to the observed output fringe $\langle N \rangle$ (panel a) yields a mean atom number of $n_s = 3.9 \pm 0.1$ consistent with an independent fit to the variance $\langle (\Delta N)^2 \rangle$ (panel b), which predicts $n_s = 3.8 \pm 0.1$. Most importantly a fit of the theoretically expected form (18) with n_s as free parameter yields an average atom number of $n_s = 4.4 \pm 1.3$ inside the interferometer. Each data point comprises about 200 individual measurements. Panel d) shows a zoom-in of the observed sensitivity around $\varphi = \pi$. We observe sub-shot noise

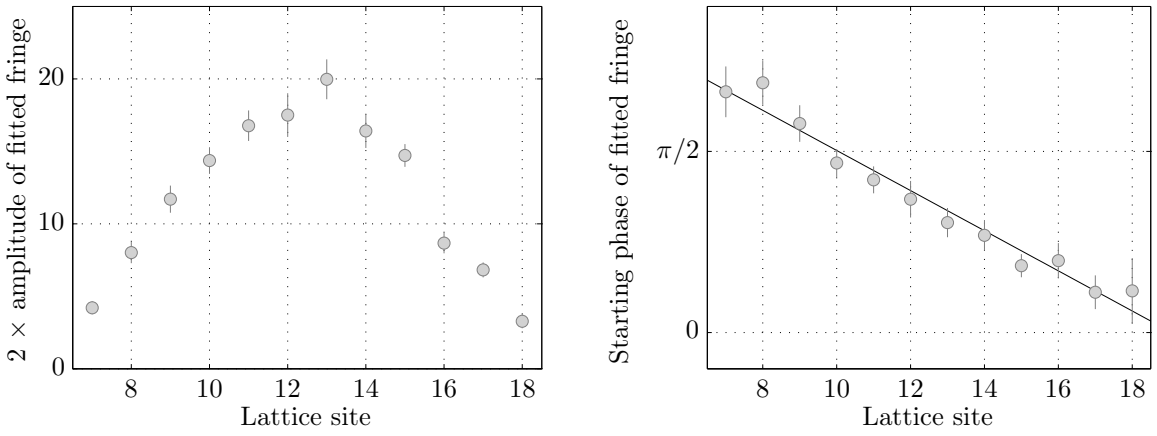

.

Figure 22: SU(1,1) Interferometer in a one-dimensional lattice. Due to a power gradient of the applied microwave, each lattice well experiences a slightly different level shift. **a)** shows the modulation of the fitted side mode population $\langle N \rangle$ obtained after the interferometer for an evolution time of 140 ms in each beam splitter. **b)** The phase of the output fringe varies linearly with lattice position. This data has been extracted from measurements comprising four full periods of the signal, like those shown in Figure 18

performance. All error bars are 1σ and are reduced compared to the previous measurement as a result of more experimental realizations shrinking the statistical error on the variance measurements. This statistical error is predominant.

Pictures of empty side modes (see Figure 24) are recorded interleaved with the SU(1,1) interferometer, as discussed above. The error on estimating the detection noise is included into the measurement of the phase sensitivity but play only a minor role.

However, the experimentally observed phase sensitivity relies crucially on the subtraction of the mean detection noise. Although this contribution is well characterized and included into the error budget it might appear refutable – especially, since we could not observe sub-shot noise performance in neighbouring lattice sites. The variance at the interferometer's most sensitive point almost fully consists of detection noise and in order to extract the phase sensitivity we subtract two large numbers yielding almost zero. To circumvent this problem in the future, we will constrain ourselves to study the scaling of phase sensitivity with mean atom number inside the interferometer. This is possible without any subtraction of detection noise [45] and undisputable evidence for Heisenberg scaling might be given, rather than claiming sensitivity at the Heisenberg limit.

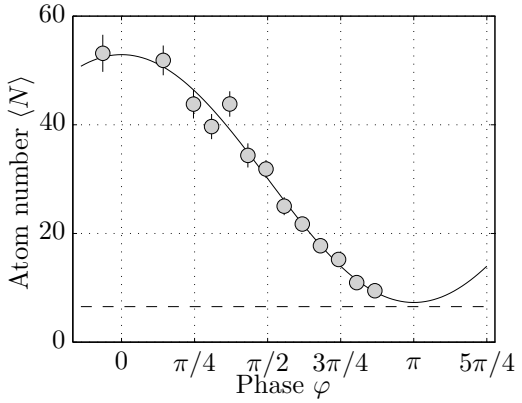

(a) side mode population at the output

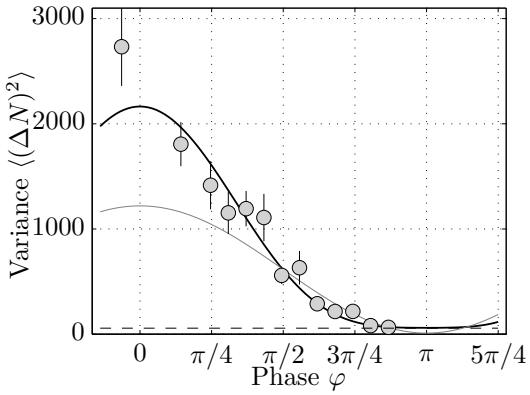

(b) side mode variance at the output

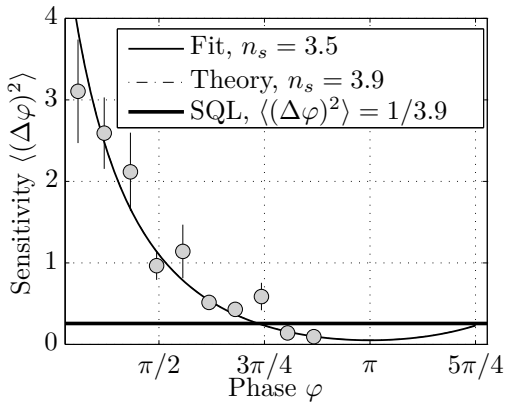

(c) Phase sensitivity

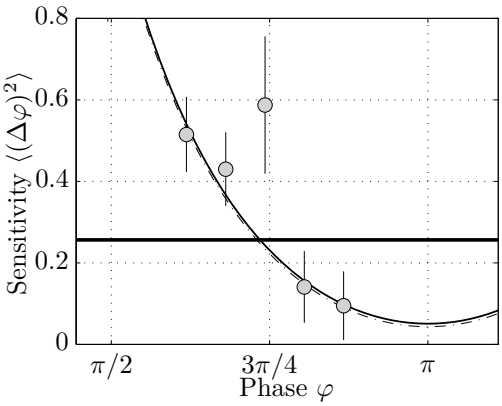

(d) Zoom in of panel c)

Figure 23: Measured phase sensitivity for an evolution time of 80 ms at magnetic field $B = 0.91$ G with stabilized microwave power. Each data point comprises more than 200 experimental realizations in a single lattice site. We post-selected experimental shots with total atom number in the range 630 ± 60 atoms, a region much larger than in the corresponding previous measurement.

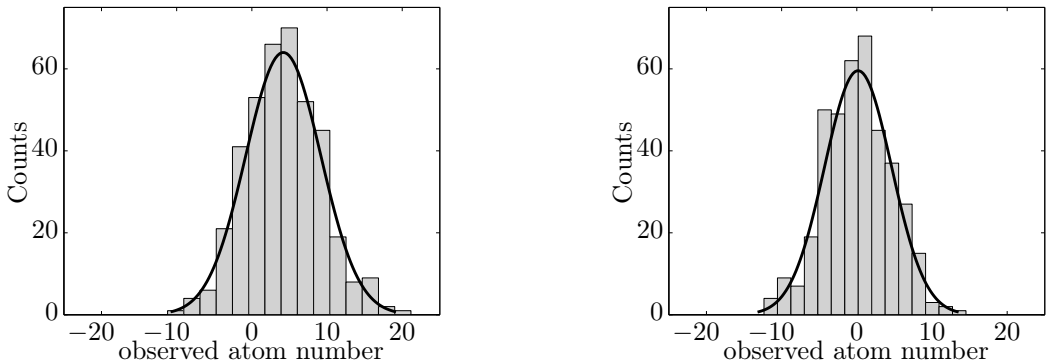

Figure 24: Characterization of detection noise for the measurement of Figure 23. Around 400 physical realizations with empty side modes have been measured interleaved with the actual SU(1,1) Interferometer. The left (right) histogram shows the observed atom number for state $|+1\rangle$ ($|-1\rangle$). The Gaussian fit gives a mean value of $\mu = 4.2 \pm 0.2$ atoms for state $|1\rangle$ and $\mu = 0.2 \pm 0.2$ atoms for state $|-1\rangle$. The atom number independent detection noise is given by its Gaussian width. We find $\sigma = 5.0 \pm 0.2$ for the left and $\sigma = 4.5 \pm 0.2$ for the right histogram.

4 Outlook

We have presented the implementation of an active SU(1,1) interferometer harnessing spin-exchange in a Bose-Einstein condensate. A controlled period of spin-changing collisions acts as an active beam splitter. During this time entangled atom pairs are produced. By accessing the differential phase the spin-changing collisions have been inverted and a beam combiner has been implemented. We characterized the individual processes as well as the overall performance of the SU(1,1) interferometer. Both the beam splitter as well as the beam combiner are non-linear elements.

The SU(1,1) interferometer has been studied in particular with focus on its phase sensitivity. Only very recently has such an interferometer been realized with photons, but in a purely classical framework with no access to phase sensitivity [47]. We observed phase sensitivity exceeding the classical shot-noise limit in accordance with the theoretical prediction. However a systematic study is still pending and will be the focus of future work. In particular we want to investigate the phase sensitivity for different mean atom numbers inside the interferometer. The experimentally obtained phase sensitivity relies crucially on the subtraction of detection noise and performance at the Heisenberg limit $\langle(\Delta\varphi)^2\rangle = 1/n_s^2$ can only be inferred. The weaker statement of Heisenberg scaling, $\langle(\Delta\varphi)^2\rangle \propto 1/n_s^2$, however, is directly accessible even with imperfect detection. So far the reasons for not observing sub-shot noise performance in the entire optical lattice remain unresolved, but we believe that compelling evidence for Heisenberg scaling can be obtained in this system.

In a next step we want to realize the SU(1,1) interferometer in its original proposal. Instead of varying the phase of the pump mode as we did in this proof-of-principle scheme we intend to introduce a differential phase between the side modes by applying microwave dressing to one of the arms. Then the pump mode is only shifted by a constant phase of $\pi/2$ and the sensitivity can be recorded by varying the phase φ_s between both side modes.

The ability to observe already small average atom numbers (on the order of one atom per arm) inside the interferometer is due to the non-linear amplifiers. Instead of incorporating these into an interferometer we are also considering to utilize them in general for non-linear read out. It is planned to improve our current setup with single atom resolution [48].

In quantum optics parametric down-conversion opened up a cornucopia of new perspectives: Experiments questioning the foundations of quantum mechanics arose from it as well as it constitutes the corner stone for applications of photonic entanglement [42, 49]. The same might become true for spin-exchange generating entanglement in the realm of massive particles. For instance EPR correlations [50, 51] and Bell's inequality [49] might become experimentally accessible.

References

[1] W. K. Wootters, Phys. Rev. D **23**, 357 (1981).

[2] S. L. Braunstein and C. M. Caves, Phys. Rev. Lett. **72**, 3439 (1994).

[3] M. Nielsen and I. Chuang, *Quantum Computation and Quantum Information* (Cambridge University Press, 2000).

[4] S. L. Braunstein and G. J. Milburn, Phys. Rev. A **51**, 1820 (1995).

[5] V. Giovannetti, S. Lloyd, and L. Maccone, Phys. Rev. Lett. **96**, 010401 (2006).

[6] L. Pezzé and A. Smerzi, Phys. Rev. Lett. **102**, 100401 (2009).

[7] V. Giovannetti, S. Lloyd, and L. Maccone, Nat Photon **5**, 222 (2011).

[8] B. Yurke, S. L. McCall, and J. R. Klauder, Phys. Rev. A **33**, 4033 (1986).

[9] S. L. Rolston and W. D. Phillips, Nature **416**, 219 (2002).

[10] P. Meystre, *Atom Optics* (Springer, 2001).

[11] H. Lee, P. Kok, and J. P. Dowling, Journal of Modern Optics **49**, 2325 (2002).

[12] A. D. Cronin, J. Schmiedmayer, and D. E. Pritchard, Rev. Mod. Phys. **81**, 1051 (2009).

[13] B. Lücke, M. Scherer, J. Kruse, L. Pezzé, F. Deuretzbacher, P. Hyllus, O. Topic, J. Peise, W. Ertmer, J. Arlt, L. Santos, A. Smerzi, and C. Klempt, Science **334**, 773 (2011).

[14] S. R. Leslie, J. Guzman, M. Vengalattore, J. D. Sau, M. L. Cohen, and D. M. Stamper-Kurn, Phys. Rev. A **79**, 043631 (2009).

[15] C. Klempt, O. Topic, G. Gebreyesus, M. Scherer, T. Henninger, P. Hyllus, W. Ertmer, L. Santos, and J. J. Arlt, Phys. Rev. Lett. **104**, 195303 (2010).

[16] H. Strobel, W. Muessel, D. Linnemann, T. Zibold, D. B. Hume, L. Pezzé, A. Smerzi, and M. K. Oberthaler, "Atomic entanglement beyond spin squeezing detected via Fisher Information," (2014), to appear soon.

[17] W. Muessel, H. Strobel, M. Joos, E. Nicklas, I. Stroescu, J. Tomkovic, D. B. Hume, and M. K. Oberthaler, Applied Physics B **113**, 69 (2013).

[18] R. Grimm, M. Weidemüller, and Y. B. Ovchinnikov, Advances in atomic, molecular, and optical physics **42**, 95 (2000).

[19] D. M. Stamper-Kurn and M. Ueda, Rev. Mod. Phys. **85**, 1191 (2013).

[20] Y. Kawaguchi and M. Ueda, Physics Reports **520**, 253 (2012).

[21] T. Ohmi and K. Machida, Journal of the Physical Society of Japan **67**, 1822 (1998).

[22] T.-L. Ho, Phys. Rev. Lett. **81**, 742 (1998).

[23] C. K. Law, H. Pu, and N. P. Bigelow, Phys. Rev. Lett. **81**, 5257 (1998).

[24] R. B. Diener and T.-L. Ho, ArXiv e-prints (2006), cond-mat/0608732 .

[25] G. I. Mias, N. R. Cooper, and S. M. Girvin, Phys. Rev. A **77**, 023616 (2008).

[26] R. J. Lewis-Swan and K. V. Kheruntsyan, Phys. Rev. A **87**, 063635 (2013).

[27] H. Strobel, *Quantum Spin Dynamics in Mesoscopic Bose-Einstein Condensates*, Master's thesis, University of Heidelberg (2011).

[28] J. Kronjäger, C. Becker, P. Navez, K. Bongs, and K. Sengstock, Phys. Rev. Lett. **97**, 110404 (2006).

[29] E. M. Bookjans, C. D. Hamley, and M. S. Chapman, Phys. Rev. Lett. **107**, 210406 (2011).

[30] F. Gerbier, A. Widera, S. Fölling, O. Mandel, and I. Bloch, Phys. Rev. A **73**, 041602 (2006).

[31] S. Haroche and J. Raimond, *Exploring the Quantum: Atoms, Cavities, and Photons*, Oxford Graduate Texts (OUP Oxford, 2006).

[32] W. Petrich, M. H. Anderson, J. R. Ensher, and E. A. Cornell, Phys. Rev. Lett. **74**, 3352 (1995).

[33] A. J. Leggett, Rev. Mod. Phys. **73**, 307 (2001).

[34] C. Gerry and P. Knight, *Introductory Quantum Optics* (Cambridge University Press, 2005).

[35] G. Agarwal, *Quantum Optics*, Quantum Optics (Cambridge University Press, 2012).

[36] U. Leonhardt, *Essential Quantum Optics: From Quantum Measurements to Black Holes* (Cambridge University Press, 2010).

[37] P. D. Nation, J. R. Johansson, M. P. Blencowe, and F. Nori, Rev. Mod. Phys. **84**, 1 (2012).

[38] D. Han and Y. S. Kim, Phys. Rev. A **37**, 4494 (1988).

[39] S. Baskal, E. Georgieva, Y. S. Kim, and M. E. Noz, Journal of Optics B: Quantum and Semiclassical Optics **6**, S455 (2004).

[40] V. Giovannetti, S. Lloyd, and L. Maccone, Science **306**, 1330 (2004).

[41] R. Horodecki, P. Horodecki, M. Horodecki, and K. Horodecki, Rev. Mod. Phys. **81**, 865 (2009).

[42] S. L. Braunstein and P. van Loock, Rev. Mod. Phys. **77**, 513 (2005).

[43] R. Islam, C. Senko, W. C. Campbell, S. Korenblit, J. Smith, A. Lee, E. E. Edwards, C.-C. J. Wang, J. K. Freericks, and C. Monroe, Science **340**, 583 (2013).

[44] Y. Shaked, R. Pomerantz, and A. Peer, ArXiv e-prints (2012), arXiv:1209.4194 [physics.optics] .

[45] A. M. Marino, N. V. Corzo Trejo, and P. D. Lett, Phys. Rev. A **86**, 023844 (2012).

[46] R. G. Miller, Biometrika **61**, 1 (1974).

[47] J. Jing, C. Liu, Z. Zhou, Z. Y. Ou, and W. Zhang, Applied Physics Letters **99**, 011110 (2011).

[48] D. B. Hume, I. Stroescu, M. Joos, W. Muessel, H. Strobel, and M. K. Oberthaler, Phys. Rev. Lett. **111**, 253001 (2013).

[49] J.-W. Pan, Z.-B. Chen, C.-Y. Lu, H. Weinfurter, A. Zeilinger, and M. Żukowski, Rev. Mod. Phys. **84**, 777 (2012).

[50] M. D. Reid, P. D. Drummond, W. P. Bowen, E. G. Cavalcanti, P. K. Lam, H. A. Bachor, U. L. Andersen, and G. Leuchs, Rev. Mod. Phys. **81**, 1727 (2009).

[51] C. Gross, H. Strobel, E. Nicklas, T. Zibold, N. Bar-Gill, G. Kurizki, and M. K. Oberthaler, Nature **480**, 219 (2011).

„Das Werk ist die Totenmaske der Konzeption“ schrieb einst Walter Benjamin. Ich hoffe, dass diese Arbeit dem Benjamin'schen Diktum entschieden widerspricht: Nichts Vollendetes, Abgeschlossenes soll sie darstellen und auch keine Reduktion der Möglichkeiten, sondern ganz im Gegenteil den Blick auf die Zukunft lenken mit all ihren Chancen. Insbesondere sollte diese Master-Arbeit nicht mit einer abschließenden Abschlussarbeit verwechselt werden. Das Narrativ in das sich diese Arbeit vielleicht einmal einordnen wird, muss erst noch gefunden werden.

Es ist offensichtlich, dass diese Arbeit das Ergebnis eines Gruppenprojekts ist, an dem viele beteiligt sind und das ohne jeden einzelnen unmöglich wäre.

Ich möchte besonders Markus Oberthaler danken, dass er mich so enthusiastisch in seine Gruppe aufgenommen hat und mir die außergewöhnlich Möglichkeit eröffnet hat, den in dieser Arbeit gestellten Fragestellungen auch in Zukunft gemeinsam nachzugehen. Dieser Vertrauensvorschuss und sein Engagement ermöglichen eine Arbeitsatmosphäre von der andere nur träumen können.

- „Meinen“ beiden Doktoranden Helmut und Wolfgang danke ich für die unermüdliche Unterstützung zu jeder Tag- und Nachtzeit. Ohne Sie wäre diese Arbeit nach dem Deckblatt leer!
- Jonas danke ich für die vielen interessanten Diskussionen und die gemeinsame Zeit im Labor.
- Eike habe ich es zu verdanken, dass ich in dieser Arbeitsgruppe gelandet bin. Außerdem hat seine Übungsgruppe mein Interesse an den kalten Atomen erst geweckt.
- Dave hat mit seinen unterschiedlichen Sichtweisen jederzeit die Gruppe bereichert und mir viel (nicht nur) aus der Welt der geladenen Teilchen beigebracht.
- Ion danke ich für die vielen spannenden Diskussionen.
- Jiris unerschöpfliches Matlab-Wissen war jederzeit nützlich.

Den NaLis danke ich für das solidarische Miteinander im Keller, Büro und Botanik. Großer Dank geht auch an die AEgIS und ATTAs für die vielen gemeinsamen Unternehmungen.

Erklärung

Ich versichere, dass ich diese Arbeit selbstständig verfasst habe und keine anderen als die angegebenen Quellen und Hilfsmittel benutzt habe.

Heidelberg, den 20.12.2013 .....